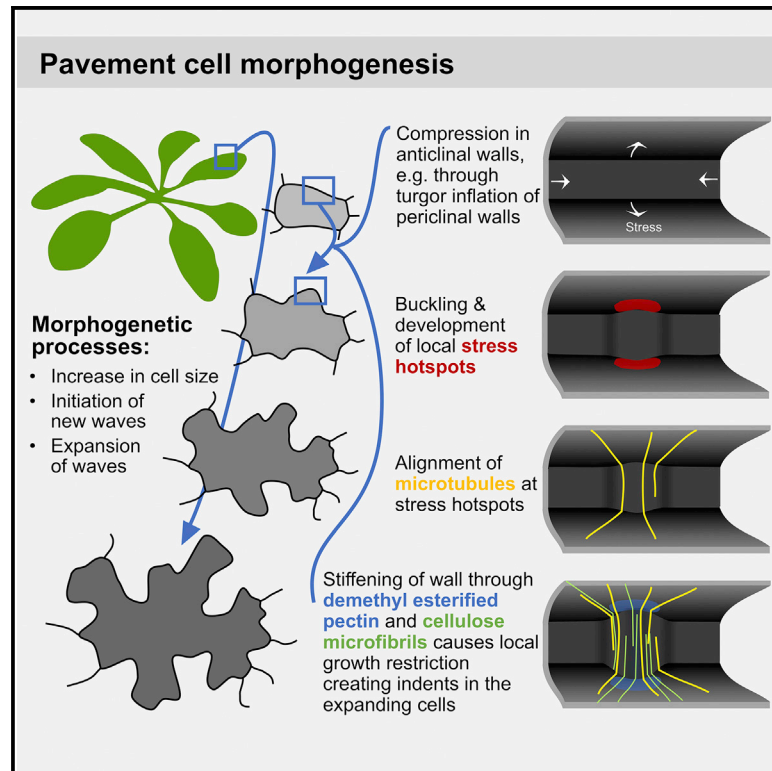# Mechanical Stress Initiates and Sustains the Morphogenesis of Wavy Leaf Epidermal Cells

Graphical Abstract

Authors

Amir J. Bidhendi, Bara Altartouri,
Frédérick P. Gosselin, Anja Geitmann

Correspondence

geitmann.aes@mcgill.ca

In Brief

Plant epidermal pavement cells often exhibit wavy shapes. A mechanical model by Bidhendi et al. predicts local mechanical heterogeneity to underlie wavy morphogenesis, preceded by buckling triggering microtubule polarization. A positive feedback loop involves polarized deposition of cellulose microfibrils and pectin de-esterification stiffening cell wall regions at indentation sides of waves.

Highlights

- Mechanical model explains shaping of wavy plant cells

- A multistep mechano-chemical process is involved in pavement cell morphogenesis

- Microtubules, cellulose, and de-esterified pectin are locally enriched

- Cell wall buckling may precede microtubule polarization

Mechanical Stress Initiates and Sustains the Morphogenesis of Wavy Leaf Epidermal Cells

Amir J. Bidhendi,[1,2] Bara Altartouri,[2] Frédérick P. Gosselin,[3] and Anja Geitmann[1,2,4,5,*]

[1]Department of Plant Science, McGill University, Macdonald Campus, 21111 Lakeshore, Ste-Anne-de-Bellevue, Québec H9X 3V9, Canada
[2]Institut de Recherche en Biologie Végétale, Département de Sciences Biologiques, Université de Montréal, Montréal, Québec H1X 2B2, Canada
[3]Laboratoire de Mécanique Multi-échelles, Département de Génie Mécanique, Polytechnique Montréal, C.P. 6079, Succ. Centre-ville, Montréal, Québec H3C 3A7, Canada
[4]Twitter: @GeitmannLab
[5]Lead Contact
*Correspondence: geitmann.aes@mcgill.ca
https://doi.org/10.1016/j.celrep.2019.07.006

SUMMARY

Pavement cells form wavy interlocking patterns in the leaf epidermis of many plants. We use computational mechanics to simulate the morphogenetic process based on microtubule organization and cell wall chemistry. Based on the *in silico* simulations and experimental evidence, we suggest that a multistep process underlies the morphogenesis of pavement cells. The *in silico* model predicts alternatingly located, feedback-augmented mechanical heterogeneity of the periclinal and anticlinal walls. It suggests that the emergence of waves is created by a stiffening of the emerging indented sides, an effect that matches cellulose and de-esterified pectin patterns in the cell wall. Further, conceptual evidence for mechanical buckling of the cell walls is provided, a mechanism that has the potential to initiate wavy patterns *de novo* and may precede chemical and geometrical symmetry breaking.

INTRODUCTION

During differentiation of plant organs, cells assume a kaleidoscopic array of morphologies depending on their location and function. Morphodynamics of plant cells is intimately linked to the mechanics of the extracellular matrix—the cell wall. Turgor, the hydrostatic pressure driving plant cell expansive growth, is balanced by the compliance of the cell wall. To grow into complex shapes, plant cells must, therefore, modulate the local mechanical properties of the wall. The cell wall of growing plant cells, the primary wall, is a composite material comprising several types of polysaccharides, proteins, ions, and water. Two main polysaccharides of the cell wall are pectins and cellulose (Cosgrove, 2018, 2016; Bidhendi and Geitmann, 2016). Cellulose microfibrils are generally recognized as the main load-bearing components of the cell wall conferring anisotropy (Crowell et al., 2011; Anderson et al., 2010; Burgert and Fratzl, 2009; Baskin, 2005). While pectin chemistry is suggested to modulate the local stiffness of the wall matrix (Carter et al., 2017; Torode et al., 2018; Bidhendi and Geitmann, 2016; Giannoutsou et al., 2016; Braybrook and

Peaucelle, 2013), our understanding of its mechanical role in cell morphogenesis is only emerging. The correlation between plant cell mechanics and morphogenesis has hitherto mostly been investigated in cells with simple shapes such as pollen tubes (Fayant et al., 2010), root hairs (Shaw et al., 2000), trichome branches (Yanagisawa et al., 2015), or cells of hypocotyl epidermis (Bou Daher et al., 2018; Peaucelle et al., 2015; Baskin, 2005). How plant cells form complex shapes is less well understood (Geitmann and Ortega, 2009).

Epidermal pavement cells form interlocking protrusions and indents in many plant species (Vőfély et al., 2019), resulting in jigsaw puzzle-like patterns (Figure 1A). Their shapes and accessibility at the organ surface make them an ideal model to study complex cell morphogenesis in plants (Bidhendi and Geitmann, 2018; Eng and Sampathkumar, 2018; Sapala et al., 2018; Majda et al., 2017; Bidhendi et al., 2015; Jacques et al., 2014; Szymanski, 2014; Mathur, 2004). Various biomechanical concepts have been proposed to explain lobe formation in pavement cells (Sapala et al., 2018; Majda et al., 2017; Jacques et al., 2014; Korn, 1976; Korn and Spalding, 1973; Watson, 1942). Hypotheses range from bending of the cell walls resulting from the growth of cells in a confined space, to inhibition of pavement cell expansion due to forces from cuticle or inner mesophyll layers, to the localized outgrowth of the anticlinal cell walls (Korn, 1976). The "localized outgrowth" hypothesis is the most widely accepted explanation for shape generation in pavement cells. It states that regions of localized outgrowth penetrate neighboring cells (Korn, 1976). However, it does not elucidate how localized outgrowth is initiated and sustained and how its subcellular position is determined. In pavement cells, microtubules and actin microfilaments are correlated with sites of necks and lobes, respectively (see Figure 1B for definitions). Both cytoskeletal arrays have been proposed to be regulated by auxin-mediated antagonistic pathways (Xu et al., 2010; Fu et al., 2005, 2002), although new evidence suggests that these signaling pathways warrant further investigation (Belteton et al., 2018). While details about their specific roles in the shaping of pavement cells are elusive, actin microfilaments and microtubules appear to be instrumental (Zhang et al., 2011; Mathur, 2006, 2004; Smith and Oppenheimer, 2005; Smith, 2003), deduced from pavement cell shape defects resulting from pharmacological and mutation-mediated interference with cytoskeletal functioning (Baskin et al., 2004, 1994; Mathur, 2004). Actin microfilament patches are
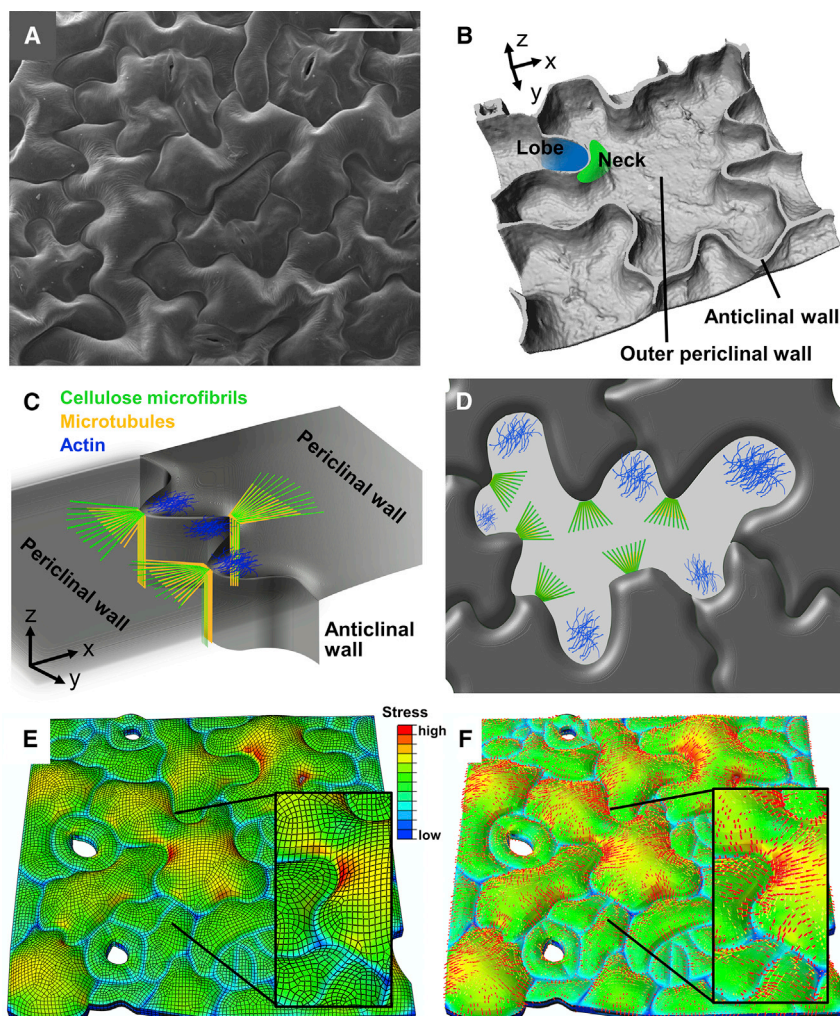
Figure 1. Pavement Cells in the Leaf Epidermis of *A. thaliana* Form Wavy Shapes
(A) SEM micrograph showing jigsaw-puzzle-shaped pavement cells (Scale bar: 30 μm).
(B) A 3D reconstruction of a confocal z stack of a pavement cell comprising the outer periclinal and anticlinal walls.
(C) Local deposition of cellulose microfibrils (green) guided by microtubules (yellow) on anticlinal and periclinal walls, proposed by Panteris and Galatis (2005). Actin arrays (blue) may be present in lobes.
(D) Paradermal schematic view of pavement cells showing localization of microtubules, cellulose microfibrils, and actin microfilaments.
(E and F) FE model of pavement cells of *Arabidopsis* cotyledon under internal pressure. Pavement cell outlines were acquired from a confocal micrograph.
(E) Neck sides of undulations show higher stresses. At identical pressures, larger cells showed more pronounced out-of-plane bulges than smaller cells.
(F) Orientation of maximum principal stress field in the epidermis as a result of cell shape and turgidity. Stress lines in periclinal walls radiate from necks.

conditions has not been investigated in *Arabidopsis* pavement cells. Sampathkumar et al. (2014) modeled the effect of pavement cell shape on the stress state of the cell wall and microtubule reorganization, and a causal link is made between cell shape and the spatial orientation of microtubules. However, while this relationship may constitute one step of a patterning mechanism, it does not explain the wave formation *de novo* or the reverse question of the effect of microtubule (or cellulose microfibril) orientation on shape development. Majda et al. (2017, 2019) proposed that stretching of the anticlinal walls with heterogeneous stiffness underlies border waviness in pavement cells, an original mechanical morphogenetic model that we have assessed elsewhere (Bidhendi and Geitmann, 2019a) and showed to be incompatible with known concepts of pavement cell morphogenesis.

The finite element (FE) method is a mathematical tool widely used in structural mechanics to solve problems involving complex materials and geometries (Bidhendi and Geitmann, 2018, 2019b). We developed FE-based mechanical models to investigate the mechanics involved in the formation of wavy patterns starting from simple polygonal cell geometries. The spatial distribution of putative mechanical agents including pectin, cellulose, and microtubules supports the *in silico* predictions.

RESULTS

Verifiable Predictions for Cell Wall Deformation through Finite Element Modeling

Since apparent waviness of leaf pavement cells corresponds to bends in the anticlinal wall, the deformation of this wall has been the primary focus of many experimental or modeling studies

suggested to promote local outgrowth in lobes through exocytotic delivery of new wall-building materials and wall-loosening agents (Cosgrove, 2005; Panteris and Galatis, 2005; Smith, 2003; Fu et al., 2002). Microtubules are generally thought to regulate cell wall mechanics by guiding the location of insertion and trajectory of cellulose synthase (CESA) enzymes (Gu et al., 2010; Hamant and Traas, 2010; Crowell et al., 2009). Therefore, microtubule distribution is sometimes used as a proxy to infer the orientation of cellulose microfibrils. Crucially, microtubule orientation is also indicative of the orientation of subcellular stress fields and may act as a stress sensor (Hamant et al., 2019; Landrein and Hamant, 2013).

Panteris and Galatis (2005) proposed that actin filaments are predominantly present in lobes promoting their expansion and that a cortical microtubule array is associated with the anticlinal wall (wall perpendicular to epidermis plane; Figure 1B) of a neck flaring out under the periclinal wall (Figures 1C and 1D). They postulate that cellulose mirrors this microtubule array, resulting in a stiffening of the cell wall in necks. Mechanical validation of this concept is lacking, however (Jacques et al., 2014). The role of the wall polysaccharides in mediating the mechanical
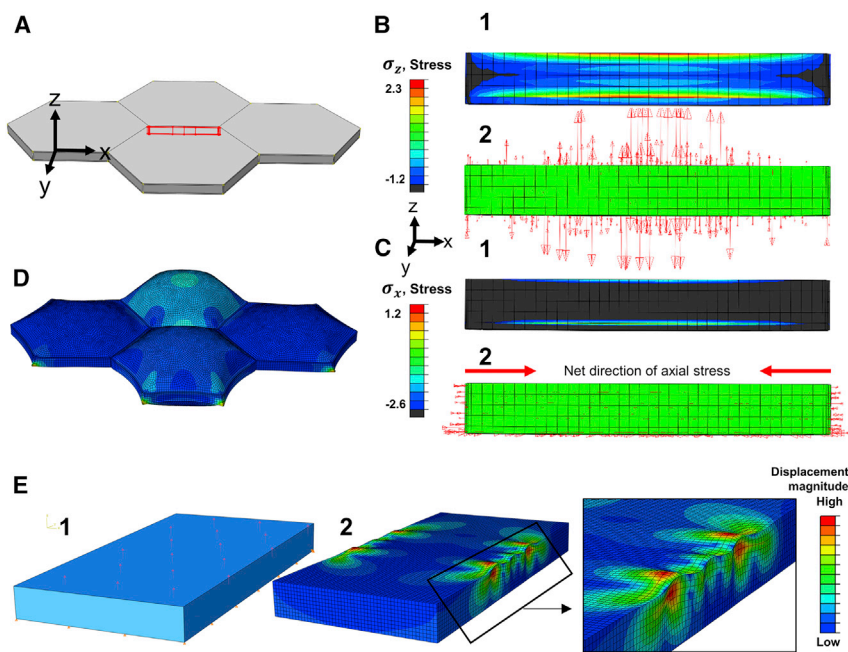
Figure 2. FE Simulation of Stresses and Resulting Deformations upon Application of Internal Pressure

(A) Structure of four-cell FE model used to assess stress pattern in the anticlinal wall surrounded by hexagonal cells. The red rectangle marks the anticlinal wall that is shown isolated in (B) and (C).

(B and C) In this wall, tensile stress components in the vertical direction (B) are significantly larger than in the horizontal direction (C). (B-1) Color-coded distribution of vertical (z direction) component of wall stress. (B-2) Arrows indicate the magnitude and direction of the vertical stress. (C-1) Color-coded distribution of axial (x direction) component of wall stress. (C-2) Arrows indicate axial stress in the horizontal direction, revealing that compressive stresses can result from the vertical expansion of the cells. Stress values are relative, as normalized input values are used in models (see Method Details).

(D) Deformed model in (A) after turgor application. Isotropic and uniform material properties are used. Relative turgor values are specified in Figure S1K. The periclinal wall of the cell with the higher pressure initially forms a more pronounced bulge in the z direction, pulling the anticlinal walls inward (also see Figures S1G–S1K).

(E) Model of a brick-shaped cell with pressure applied to inner face of the outer periclinal wall. Pressure was not applied to lateral walls, as equal pressures cancel each other out in a multicell context. The inner periclinal wall was prevented from outward or inward displacement to simulate attachment to the mesophyll layer (E-1). Buckling mode from the linear buckling analysis demonstrates wave formation in both periclinal and anticlinal walls. The model indicates that at the location of the indentation, the periclinal walls bulge out of the plane, consistent with microscopic observations of pavement cells (E-2).

(e.g., Sapala et al., 2018; Majda et al., 2017; Jacques et al., 2014). We have previously shown that a mechanism proposed by Majda et al. (2017, 2019) based on stretching the anticlinal wall does not produce undulations (Bidhendi and Geitmann, 2019a). Our preliminary modeling results further indicate that alternative mechanisms based solely on anticlinal walls, such as the differential expansion of the anticlinal wall and differential turgor in neighboring cells, cannot be the mechanisms underlying wave formation in pavement cells (see Method Details). Therefore, we moved toward 3D models of pavement cells that comprise both anticlinal and periclinal walls. A 3D model of pressurized epidermal cells with realistic cell geometries extracted from confocal micrographs shows that localized stress hotspots develop at the neck sides of waves on the periclinal walls (Figures 1E and 1F), consistent with Sampathkumar et al. (2014). The simulations also show that for the same pressure, larger cells bulge out more than smaller cells, as shown by Sapala et al. (2018), confirming that geometry constitutes an important element determining the mechanical behavior of these cells.

Stress in Anticlinal Walls Is Highly Anisotropic and Can Become Compressive

To examine cell wall stress, FE models of hexagonally shaped cells were developed, and turgor is applied to internal faces (Figures 2A and S1G). Upon pressurization, the periclinal walls initially bulge out and pull the anticlinal walls inward (see Figures 2D, S1K [four-cell model], and S1H−S1J [two-cell model]). The results indicate that for cell aspect ratios typical

for *Arabidopsis* epidermal cells, the turgor-driven stress in the anticlinal wall is highly anisotropic, the axial component of the stress (σ_x) can become locally negative, and the vertical component (σ_z, in the direction perpendicular to the plane of the leaf) forms the dominant tensile stress direction (Figures 2B and 2C). The generation of compressive stresses was a non-intuitive prediction and is intriguing since compression can cause buckling. For proof of concept that this may happen in anticlinal walls, we developed an FE model of a closed box with height and length dimensions typical for epidermal cells (Figure 2E-1; see Method Details). Linear buckling analysis yielded positive eigenvalues, indicating that under internal pressure, the structure can buckle under the prescribed loading direction. A buckling mode for this model is depicted in Figure 2E-2; it shows wrinkling or crimpling at the edges. Interestingly, the model suggests that the periclinal wall at the neck side of indentations bulges out locally (inset in Figure 2E-2), which is consistent with microscopic observations (Figure 1A and orthogonal view in Figure 5D [bottom]). These findings raise the perspective that simply based on cell geometry and turgor (see Figure S5G), the walls of pavement cells are prone to buckling. This is predicted despite not accounting for any additional compressive forces that can arise due to a growth mismatch between neighboring cells.

Differential Stiffness in the Periclinal Wall Can Generate Cell Border Undulations

If buckling is an initiating mechanism, it could create only rather small bends. However, it could be an initiating trigger if a
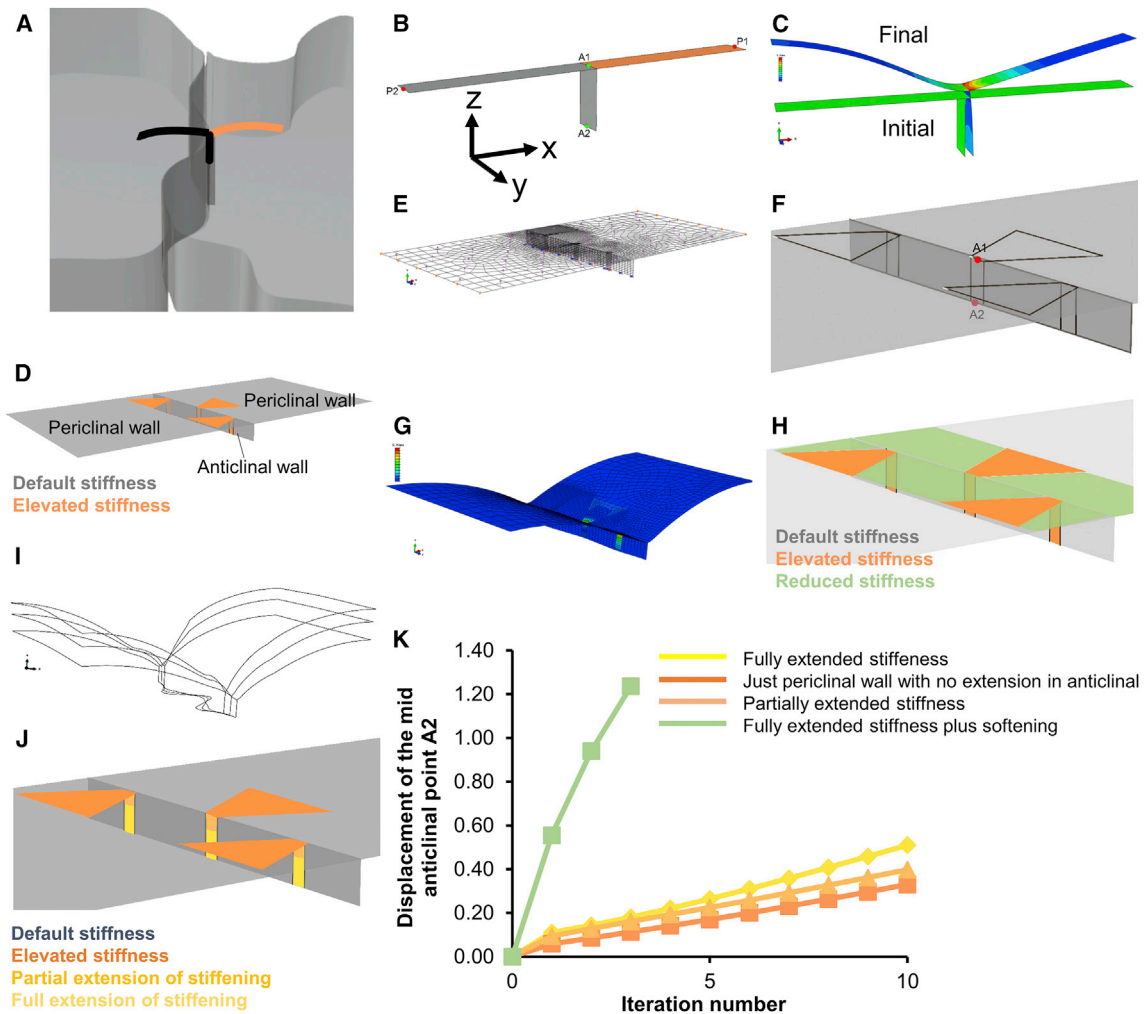
Figure 3. Model of Cell Wall Segments Containing Stiff and Soft Regions Deformed by Pressure

(A) Illustration of the position of a segment of two adjacent cells containing periclinal walls and the shared anticlinal wall used for simulations. Orange indicates higher stiffness or lower extensibility. The deformation of this segment under turgor application is modeled using the beam and shell approach.

(B) Shell model of wall segments. Pressure is applied on the lower face of the periclinal walls, similar to loading in the beam model (Figure S2A).

(C) Similar to the beam model (Figure S2B), the anticlinal wall moves toward the stiffer side.

(D) Model with alternate placement of stiffened regions on the periclinal and anticlinal walls of two adjacent cell segments.

(E) Pressure is applied to the inner face of the shell periclinal walls.

(F) Position of fiducial markers whose displacement was used to quantify the lobe formation.

(G) Initiation of undulations in the first iteration of the model. Heatmap represents von Mises stress.

(H) Model with the inclusion of softened regions between incipient necks.

(I) Evolution of undulations for three iterative load applications and stress relief.

(J) Stiffened anticlinal bands extending from the superficial border into the depth of the cell. The bands were either fully extended, spanning the anticlinal wall linking the outer and inner border, only partially extended, or absent, as illustrated with colors.

(K) Displacement of point A2 under different wall stiffening-softening scenarios reveals that stiffened anticlinal bands lead to more pronounced undulation, but the effect is small compared to that of a softer material between necks on the periclinal wall. The stiff, soft, and default regions were assigned Neo-Hookean elastic constants (C_{10}) of 10, 0.05, and 0.5, respectively.

subsequent mechanism amplifies its effect. We hypothesize that to accommodate pronounced wavy borders, the mechanical properties of the periclinal wall must vary in alternatingly arranged regions (similar to the organization of microtubules and cellulose illustrated in Figures 1C and 1D). Beam models were developed with different stiffness values for periclinal walls of two adjacent cells with a shared anticlinal wall (Figures 3A and

S2A). Under turgor, the periclinal walls bulge out (in the z direction), and the anticlinal wall moves from the midpoint toward the cell with the stiffer periclinal wall (Figure S2B). The 2D thin shell model of the same conditions (Figure 3B) yields the same results (Figures 3C, S2C, and S2D). We verified that this mechanism works independently of turgor differentials between the adjacent cells (Figure S3). At lower values, the displacement of
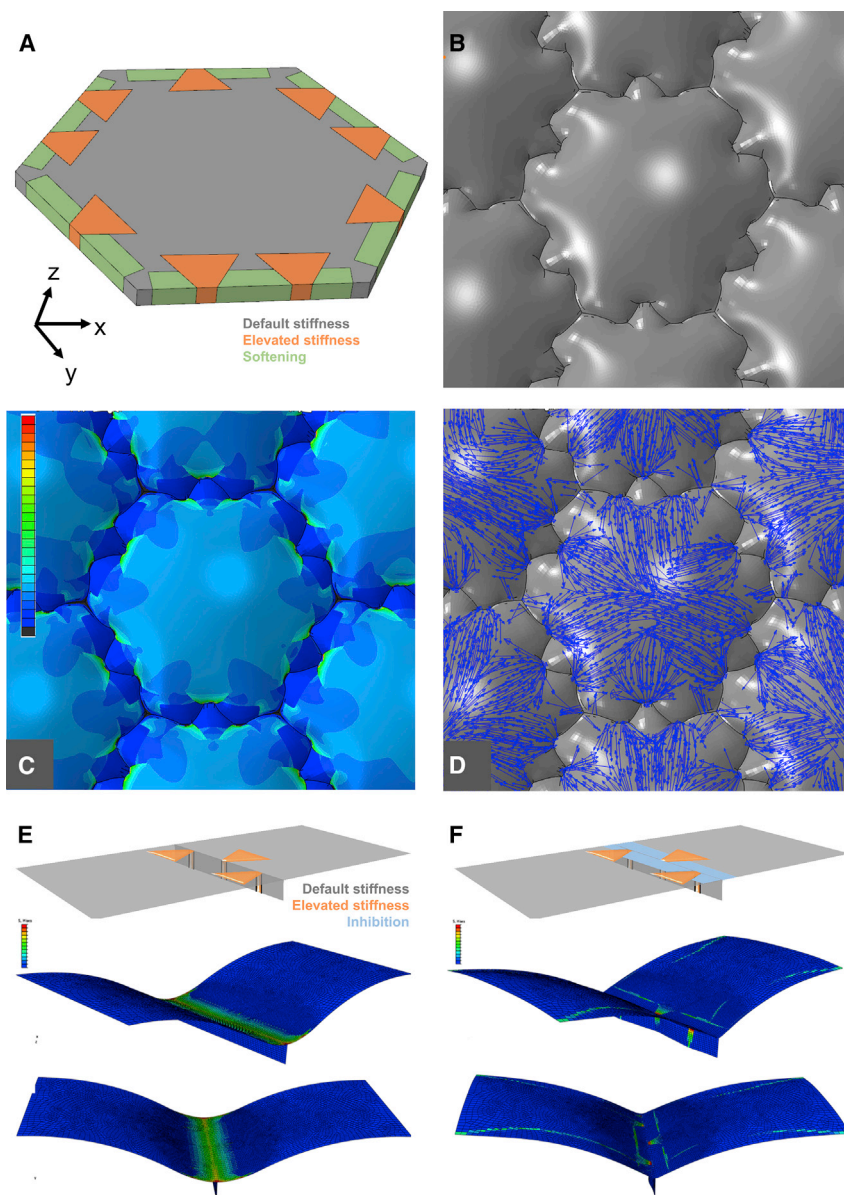
Figure 4. Shape and Stress Formation in Pavement Cells by Cell Wall Stiffness Inhomogeneity

(A) Whole-cell model with local, alternating stiffening and softening on inner and outer periclinal walls and the stiffened bands on anticlinal walls.

(B–D) Turgor-induced deformation and stress in a model composed of multiple single-cell units in (A). Turgor was set equal in all cells. (B) Formation of interlocking patterns as seen from above. (C) Stress pattern in the periclinal walls. Heatmap represents maximum principal stresses. (D) Orientation of stress lines in periclinal walls.

(E and F) Incorporation of positive stress-stiffening feedback mechanism that amplifies stiffness based on local stress, starting from a very small stiffness differential (1%) between incipient necks and adjacent regions. Deformation and stress pattern is shown after 100 iterations of the load application. Heatmap represents von Mises stress. (E) Without an inhibition mechanism, stiffness differentials even out. (F) Inhibition of stiffening at inter-neck locations allows stiffness differentials to amplify and waves to form.

turgor with stress relief at each iteration results in pronounced border waves (Figure S4D). The model also shows that inclusion of softened regions between the stiffening zones (green zones in Figure 3H) enhances the interdigitations in the *xy* plane with a reduced "ballooning" of the periclinal walls in the *z* direction, compared to the simulations without the softening (Figure 3I versus S4D). We observed that undulations can be formed without the extension of stiffening bands in the depth of the anticlinal wall (Figure 3J), but the magnitude is reduced in their absence (Figure 3K).

To assess whether the concept holds in a tissue context, a multicell model was developed by arranging a lattice of identical hexagonal cells with alternating stiffened and softened zones on the periclinal and anticlinal walls (Figure 4A). Upon pressurization, the model forms interlocking cell patterns (Figure 4B), and the highest stresses correspond to regions with higher stiffness (necks) (Figures 4C and 4D), with maximum stress lines radiating from necks, extending to adjacent necks, and crossing each other in the center of the periclinal cell wall in the case of isometric cells (Figures 4D and S4E). Moreover, upon restarting a simulation with the pressurized and inflated geometry of Figure 4D, but with homogeneous wall properties, the geometry itself generates stress heterogeneity. Upon wave initiation, even with uniform stiffness, stresses are higher on neck sides (Figure S4F). Geometry, therefore, constitutes an element in the feedback loop, further supporting our stress analysis in fully shaped pavement cells (Figures 1E and 1F) and that of Sampathkumar et al. (2014).

the anticlinal wall toward the stiffer side increases rapidly with increasing stiffness differential between periclinal walls, but at higher values, it plateaus (Figure S4A).

Interlocking Patterns with Alternate Positioning of Differential Stiffness along the Periclinal Walls

Based on the previous results, we hypothesized that border waves can be developed by alternatingly placed regions of cell wall stiffening on periclinal walls on two sides of the border, under application of turgor (Figures 3D and 3E). The horizontal (in *x* direction) displacement of the midpoint of the anticlinal wall (A2) (Figure 3F) shows that one iteration of pressure application causes a displacement of the anticlinal wall that simulates the initiation of lobes and necks (Figure 3G), with higher stresses developing at stiffened (neck) regions. Repeated application of

A Positive Mechanical Feedback Loop Based on Stress-Induced Stiffening and Lateral Inhibition Can Shape Pavement Cells

We showed that a considerable stiffness ratio between the opposing necks and lobes is required to form discernable displacements of cell borders (Figures S4A–S4C; see also Method Details). Since cells are dynamic and changes in the cell wall are gradual, we hypothesized that small stiffness differentials can form wavy borders if a positive feedback mechanism exists in which the cell wall is gradually stiffened in regions with locally elevated stress. To test this hypothesis, in each loading iteration, the model is set to update local stiffness values based on the local stress (Figure S6A; see Method Details). With an initial stiffness differential of 1%, the deformation upon the first iteration is relatively small, and during subsequent iterations, the displacement of the lobe does not increase considerably but reaches a plateau (Figure 4E). Essentially, upon the initial iterations of load application, stresses are leveled, and the feedback loop causes an increase in overall stiffness at the border of the two periclinal walls instead of sharpening the differences between lobes and necks. We, therefore, tested whether adding an inhibitory mechanism could promote an augmentation in stiffness differential during feedback iterations. To implement this, feedback-driven stiffening is prevented in regions between the incipient necks, given as an input to the feedback model (Figure 4F). The simulations show that this approach was sufficient to ensure that stiffness differentials are amplified, and lobe formation is sustained through the feedback mechanism, even when starting with small (1%) stiffness differences between future necks and lobes (Figures S6B and 4F; see also Method Details).

Experimental Validation of *In Silico* Predictions

The FE models predict that alternating changes in material properties of the cell wall can produce the interlocking pattern observed in pavement cells. To experimentally validate the model predictions, we studied the spatial distribution of two major cell wall constituents—cellulose and homogalacturonan (HG) pectin (Bidhendi and Geitmann, 2016)—in the epidermis of *Arabidopsis* cotyledons. Microtubules were also studied in their capacity as stress markers.

Pectin Is Weakly Esterified on the Neck Side

Pectin de-esterification has been linked to changes in the stiffness of the plant cell wall (Bou Daher et al., 2018; Carter et al., 2017; Amsbury et al., 2016; Bidhendi and Geitmann, 2016; Peaucelle et al., 2015; Braybrook and Peaucelle, 2013; Chebli et al., 2012). To investigate possible variations in HG pectin in pavement cell walls (Bidhendi et al., 2015), we used COS[488], an oligosaccharide probe conjugated with Alexa Fluor 488, reported to be highly specific for de-esterified HG pectin (Mravec et al., 2014). Cotyledon pavement cells of wild-type (WT) *A. thaliana* from seedlings at 2–5 days after germination (DAG) were stained with COS[488] and observed under the confocal laser scanning microscope (see Method Details). The COS[488] signal exhibited variations along the profile of cell borders at the anticlinal walls (Figure 5A). Maximum intensity projections of z stacks indicated a consistent, higher affinity of COS[488] with the neck sides of waves on periclinal walls (p < 0.0001; see Quantification and Statistical Analysis and Figures 5B and S7H). This association was not limited to mature cells or pronounced waves. We observed a similar pattern of higher signals at necks even for slight curvatures (Figure 5C). Because of the challenges of working with early-stage cells, we focused on specimens at 2–5 DAG. At this stage, pavement cells are already wavy but continue to grow and form new lobes (Zhang et al., 2011). COS[488] staining also showed bright spots at cell junctions (Figure 5A). We hypothesize that de-esterification of pectin in the middle lamella at the junctions may enhance cell adhesion. This observation is similar to a study by Carter et al. (2017), who also found a higher COS[488] signal at the poles of guard cells and associated this with polar stiffening of these cells.

Rounds et al. (2011) suggested that propidium iodide, a general probe for the cell wall, has a higher affinity for weakly esterified pectin. Similar to COS[488], the propidium iodide fluorescent signal intensity oscillated along the meandering borders of pavement cells (Figure S5A). Consistently, maximum projections of z stacks showed higher signal intensities on the neck sides, while at the lobe sides, the signal was dim, and the difference was significant (Figures 5D and S5B; p < 0.0001; see Quantification and Statistical Analysis). The same observation was made analyzing orthogonal views (Figure 5D, bottom). This result is interesting, as it reinforces the possibility that propidium iodide may predominantly bind de-esterified pectin, as suggested by Rounds et al. (2011).

Cellulose Microfibrils and Microtubules Radiate from Necks

The predicted stiffening pattern in the periclinal and anticlinal walls of pavement cells can result from the deposition of cellulose microfibrils, which, in turn, is thought to be controlled by microtubules. In the GFP-MAP4 line at 2–5 DAG, microtubules beneath the outer periclinal and anticlinal walls showed a strong association with necks (Figures 6A, S5C, and S7F). In lobes, microtubules could occasionally be observed, but their occurrence was scarce, compared to necks. A similar pattern was observed for stress lines in the multicell models simulating *de novo* cell wave formation (Figures 4D and S4E) and in the model based on realistic wavy cell shapes (Figures 1E and 1F), as discussed earlier. Similar observations were made in the GFP-TUB6 line (Figures 6B, 6C, and S7D). Necks were populated with microtubules (p < 0.0001; see Quantification and Statistical Analysis), and unlike the more crowded arrays in the GFP-MAP4 line, the fan-shaped arrays were clearly distinguishable in the GFP-TUB6 line. At some locations, microtubules appeared to form bundles at locations of the cell border with only slight bends. These sites were also associated with marked accumulations of microtubule labels at the anticlinal walls (arrowheads marking the dotted microtubule on the red lines of cell borders in Figure 6B). The inner periclinal walls showed a similar trend for the microtubules at fully developed necks and for relatively straight regions corresponding to arrowheads in Figure 6B (Figure 6C). We hypothesize that these focal regions on seemingly straight wall segments mark the locations for a strain or stress-driven positive feedback loop that eventually leads to fully developed lobes and necks. We hypothesize, as will be discussed later, that this focal polarization of microtubules follows a barely
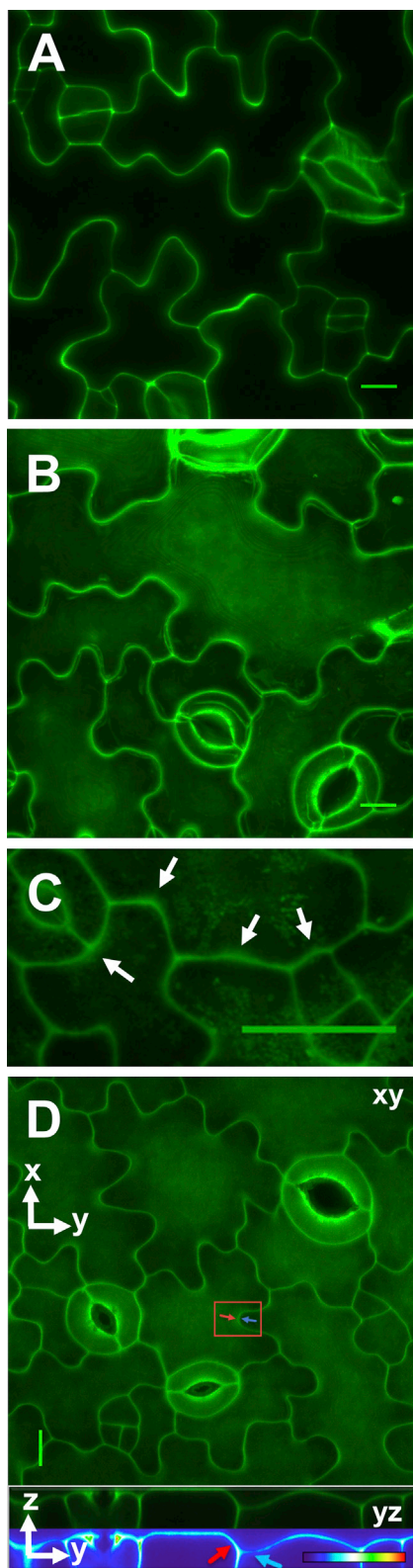
Figure 5. Staining of Pavement Cells for De-esterified HG Pectin in *A. thaliana* **Cotyledons Sampled 2−5 DAG**

De-esterified pectin, when bridged with calcium, increases cell wall stiffness.

(A) A single optical section through the center of the epidermal layer thickness stained with COS[488], specific to de-esterified pectin, shows varying signal intensity along cell borders and high signal intensity at cell junctions.

(B) Maximum projection of z stack with COS[488] staining exhibits higher signal at the neck side of the waves on periclinal walls. (p < 0.0001; n = 55 pairs of necks and lobes from 1 or 2 pavement cells per cotyledon from 5 cotyledons, from 5 seedlings were used in the analysis. See Quantification and Statistical Analysis and Figure S7H for details).

(C) Maximum projection of a sample stained with COS[488] shows that in smaller cells and along cell borders with barely developing bends, a higher signal appears at the neck side on the periclinal wall, similar to more pronounced waves as in (B).

(D) Top: maximum projection of z stack labeled with propidium iodide. Bottom: orthogonal single yz optical slice through the same z stack, crossing the center of the marked lobe and neck pair in the red rectangle (false color monochrome and heatmap). The periclinal cell wall is brighter and bulges out at the neck side but is relatively shallow and less strongly labeled at the lobe side. (p < 0.0001; n = 101 lobe and neck pairs from n = 3 to 5 pavement cells per cotyledon from 5 cotyledons. See Figure S5B and Quantification and Statistical Analysis for details.) Scale bars: 10 μm (A, B, and D) and 20 μm (C).

discernable mechanical symmetry breaking due to local cell wall buckling. Further, away from the tip of the lobes, bundles of microtubules radiating from two adjacent necks formed transverse bundles on the shank of the tube-like lobe (Figure 6A), similar to patterns of stress lines between adjacent necks in our FE models (Figures 4D and S4E). Assuming that cellulose deposition follows this pattern, lobes would be anisotropically reinforced, which would restrict their widening and facilitate their elongation, consistent with anisotropic growth patterns in pavement cells reported by Elsner et al. (2018).

In most earlier studies on pavement cells, microtubule orientation was used as a proxy for cellulose-mediated wall stiffening, presumably due to technical challenges with fluorescent labeling of cellulose proper in cotyledons. We used calcofluor white and Pontamine Fast Scarlet 4B (PFS) to stain *A. thaliana* cotyledons for cellulose (see Method Details). PFS is reported to be highly specific for cellulose (Liesche et al., 2013; Anderson et al., 2010). For both PFS and calcofluor white, a notable signal was observed in the neck regions (p < 0.0001 for PFS staining; see Quantification and Statistical Analysis) from which cellulose microfibrils appeared to radiate and form a divergent fan-shaped configuration in the outer periclinal walls (see Figures 6D−6G for calcofluor staining; and Figures S5D and S5E for PFS; Videos S1 and S2). Tips of lobes displayed considerably weaker signals. Similar to the organization of microtubules, microfibrils appeared to connect neighboring necks (Figures 6D [arrows], S5D, and S5E) and appeared mostly random in the mid-regions of cells with lower aspect ratios or were dominantly transverse in narrow cell regions (Figures 6D, 6M, and S5D−S5F). We observed that even in pavement cells of ungerminated cotyledons acquired by dissecting the seed coat, curvatures were similarly associated with radiating cellulose bundles (Figure 6G).

We hypothesized that the observed alternate cellulose deposition pattern, as predicted by our FE models, restricts the cell wall growth in necks. To investigate the mechanical impact of cellulose on wavy cell shape development, we experimentally reduced cellulose crystallinity by growing the seedlings in the
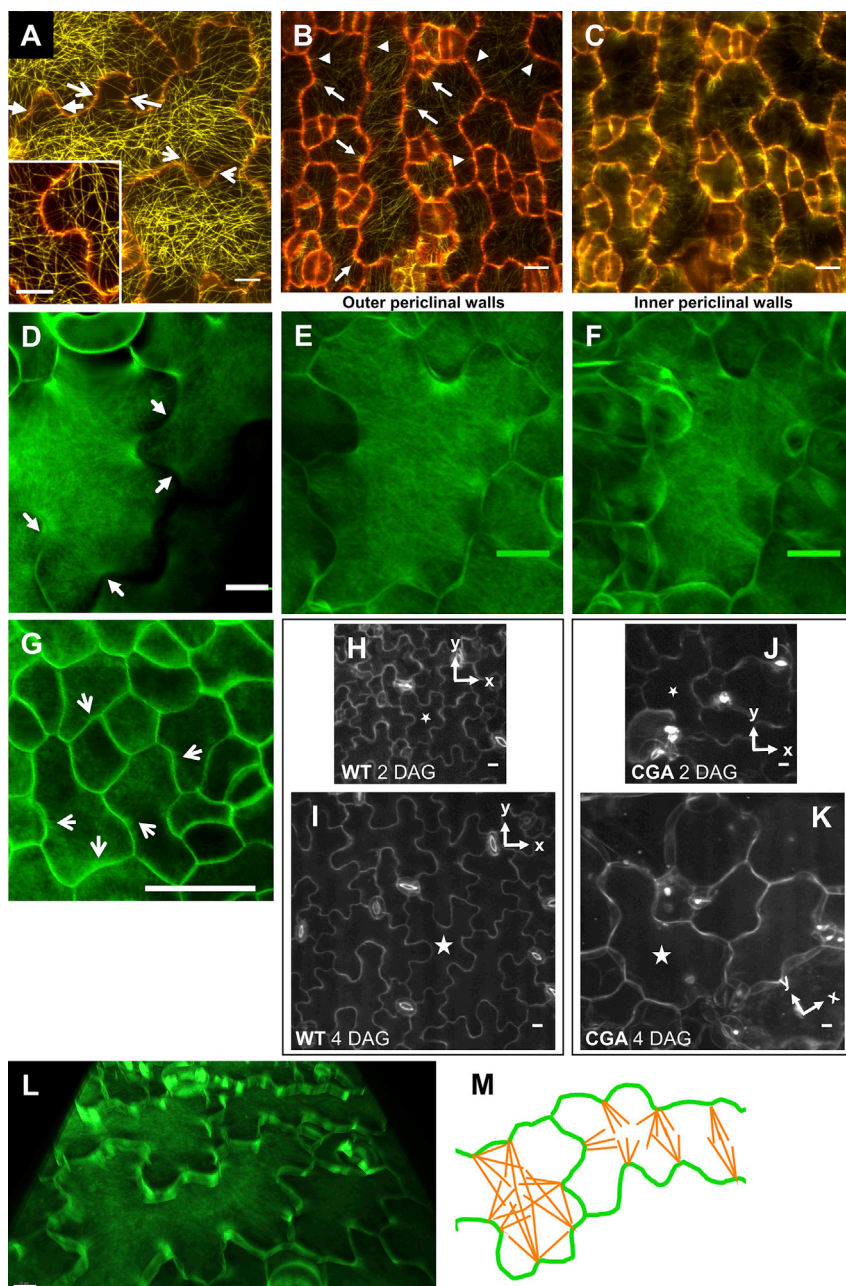
Figure 6. Organization of Microtubules (Yellow Pseudocolor) and Cellulose Microfibrils (Green Pseudocolor) in Pavement Cells of *A. thaliana* Cotyledon

(A) Microtubules in pavement cells of the GFP-MAP4 line are abundant in association with the neck sides and feature neck to neck connections forming circumferential hoops at the shank of lobes (pair of arrows, maximum projection). Inset shows higher magnification of a second sample.

(B and C) Microtubules underlying the outer and inner periclinal walls, respectively, of the same pavement cells in the GFP-TUB6 line. Micrographs are maximum projections of the top (B) and bottom (C) halves of a z stack corresponding to outer and inner periclinal walls, respectively. Microtubules were more abundant at neck sides, comparing signal intensity in selected circular regions on two sides of waves in pavement cells of the GFP-TUB6 line. (p < 0.0001; from n = 84 lobe/neck pairs from 6 pavement cells from 6 cotyledons. See Quantification and Statistical Analysis and Figure S7D.)

In (A)−(C), a single optical section from the center of the z stack was pseudocolored in red to mark cell borders.

(D−G) Calcofluor white staining for cellulose in pavement cells of *A. thaliana* cotyledons at 2−5 DAG (D−F) and extracted from seeds (G). For PFS staining of cellulose, see Figures S5D and S5E and Method Details. (D) Cellulose microfibrils are concentrated at the necks from which they radiate into the periclinal wall (maximum projection; see also Figures S5D−S5F; Videos S1 and S2). Analysis of results from PFS labeling for cellulose indicated substantially higher signal at necks (p < 0.0001; n = 88 lobe and neck pairs from 6 cells and 3 seedlings. See Quantification and Statistical Analysis for details.) Cellulose microfibrils in outer (E) and inner (F) periclinal walls of the same cells. Micrographs show maximum projections of the top (E) and bottom (F) halves of a z stack (see also Figure S5H) using calcofluor white. (G) Bundles of cellulose microfibrils in pavement cells of ungerminated cotyledon extracted from the seed coat are already associated with indentation sides of barely emerging curvatures.

(H−K) Time-lapse micrographs of pavement cell morphogenesis in WT *A. thaliana* cotyledons treated with DMSO (control) (H and I) and CGA (J and K), visualized at 2 and 4 DAG. Fluorescence is propidium iodide signal. While both samples grow in surface area and perimeter, CGA-treated cells develop fewer lobes and necks. (p < 0.001; n = 50−70 cells from 10−12 seedlings for each data point. See Quantification and Statistical Analysis and Figure S8.) The coordinate systems indicate the orientation of the mounted samples.

(L) Oblique view of 3D reconstructed z stack of pavement cells showing that cellulose microfibrils extend into the depth of the anticlinal wall at neck-lobe regions (see Videos S1 and S2; Figure S5F).

(M) Schematic representation of typical cellulose orientation depending on the cells' aspect ratio: in elongated cell regions (right), the microfibrils form a pattern predominantly perpendicular to the long axis. In cell regions with an aspect ratio close to 1 (left), bundles of cellulose are more centrifugally oriented (see also Figure 4D). Scale bars: 10 μm, 20 μm (G).

presence of CGA 325′615 (CGA; see Method Details) and monitored the shape of the same cells over 4 DAG. At 2 DAG, pavement cells of CGA-treated and control seedlings had the same perimeters and areas (see Quantification and Statistical Analysis; Figure S8). However, the formation of pronounced waves in treated specimens was significantly impeded, as they only

developed 3.3 (±0.5 SE) lobes at 2 DAG, compared to the control with 9.1 (±0.7 SE) lobes. Over the two subsequent days (at 4 DAG), cells in treated specimens added only 1 or 2 lobes, compared to 6 or 7 additional lobes in the control, despite a similar increase in cell size (p < 0.001; see Quantification and Statistical Analysis and Figure S8). These results indicate that
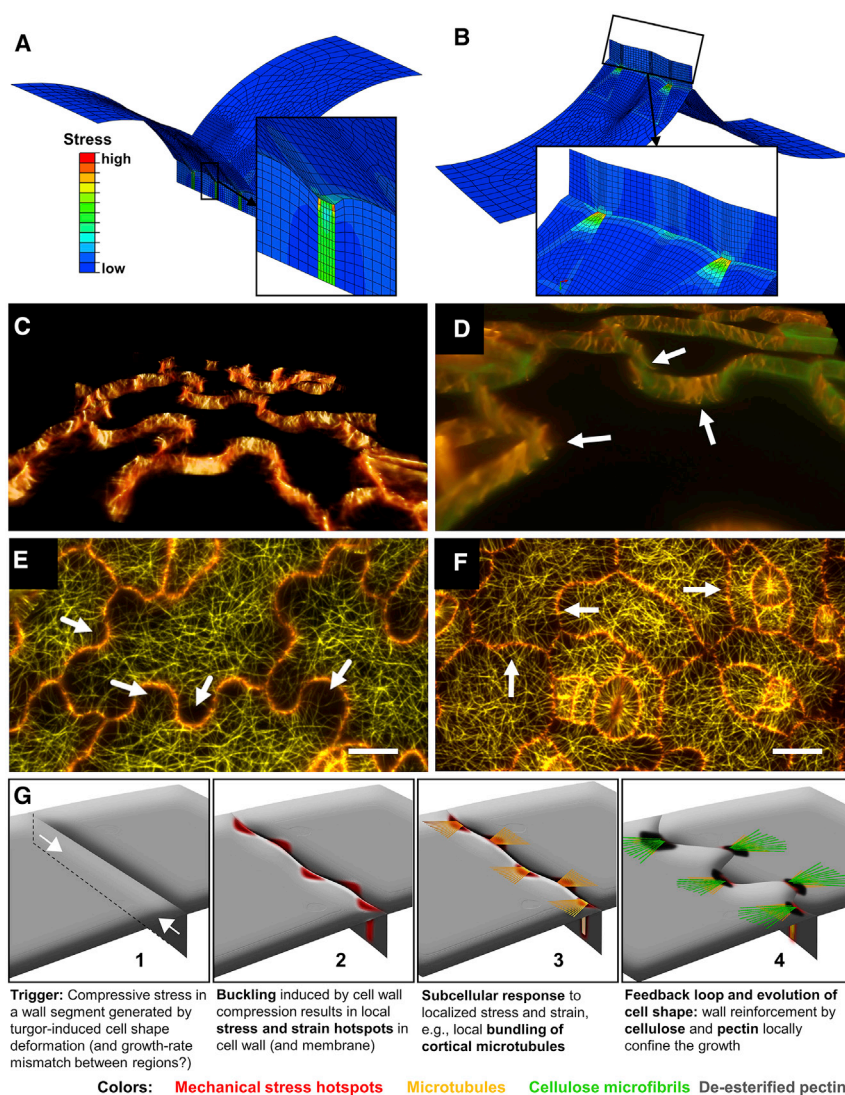
Figure 7. Patterns of Mechanical Stress and Microtubule Orientation

(A and B) FE models containing a segment of anticlinal and periclinal walls under pressure show that local stress raised in either (A) anticlinal or (B) periclinal walls is transmitted to the respective connecting wall, forming a stress coupling between the inner and outer periclinal and the connected anticlinal cell walls. In these cases, elevated stress resulted from an embedded stiffened band in each wall.

(C) Oblique view of a z stack 3D reconstruction of anticlinal cortical microtubules in pavement cells of *A. thaliana* GFP-MAP4 line.

(D) Dual-channel image of propidium iodide (green) and GFP-MAP4 (orange) showing that cortical anticlinal microtubules are more abundant at the neck side of the undulations. (p < 0.0001; determined by counting the number of microtubules on each side; n = 35 lobe and neck pairs from 9 pavement cells of 3 cotyledons of the GFP-MAP4 line. See Quantification and Statistical Analysis, Figure S7F and Video S4.)

(E and F) Maximum projections of z stacks. Cortical periclinal microtubules visualized in cotyledons of the *A. thaliana* GFP-MAP4 line at 4 (E) and 1 (F) DAG. At both stages, microtubule density at opposite sides of corresponding lobe-neck pairs is different, with higher density at the neck side. However, this difference is less pronounced at earlier developmental stages (white arrows in F pointing at microtubules on both sides). At 4 DAG (E), microtubules appear to be bundled in necks, while they are scarce in lobes. Occasionally, a few microtubules reach the tips of a lobe. The images do not correspond to the same cotyledon. Scale bars: 10 μm. A simple analysis indicates a moderate correlation between lobe curvature and microtubule density differential on two sides (see Quantification and Statistical Analysis and Figure S7G).

(G) Schematic of the proposed multistep morphogenetic mechanism of wavy shape formation. (G-1) Compressive stress in anticlinal walls arises due to internal pressure and bulging out of periclinal walls (potentially compounded by the effect of growth

mismatch between regions). (G-2) Stress and strain inhomogeneities ensued due to buckling form stress hotspots that trigger local bundling of microtubules. (G-3) Alterations in pectin esterification and reinforcement of the cell wall by cellulose deposition. Feedback mediated cellulose deposition leads to further restriction of necks and expansion of lobes (G-4).

interference with cellulose significantly reduced lobe formation from the early stages of epidermal cell development (Figures 6H−6K). This corroborates the significance of cellulose in the solidification and further development of wavy shapes by the restriction of expansion in the neck regions. We speculate that the reduced lobe number is due to flattening of early-stage lobes during cell growth in the absence of cellulose reinforcement. This finding also emphasizes that our proposed mechanism and FE predictions are not limited to cells that are already highly wavy, but also apply to lobe formation at earlier stages.

Cellulose Microfibrils and Microtubules Form Bundles at Necks that Extend to the Anticlinal Walls

We observed that cellulose enrichment and orientation seemed similar in the inner and outer periclinal walls of a given cell (Fig-

ures 6E, 6F, and S5H). This prompted us to analyze cellulose in the anticlinal walls as they link the inner and outer periclinal walls. The 3D reconstruction of calcofluor white-stained samples revealed that in neck regions, cellulose bands extend down the anticlinal walls (Figure 6L; Video S2). This can also be observed from orthogonal views of z stacks (Figures S5F-1 and S5F-2). As FE simulations show, the anticlinal extension of stiffening can act as a lever, increasing the magnitude of waves. Regardless, they might form due to the mechanical signal between the inner and outer periclinal walls and transmit it. To visualize this, we used the FE model with stiffened bands in the anticlinal, but no stiffness heterogeneity in the periclinal, walls (Figure 7A). Although this configuration does not generate any undulations as shown before, stress points are formed in the periclinal walls where they connect to the stiffened anticlinal bands. Similarly, the

stress due to local stiffening of the periclinal wall was transmitted to the anticlinal walls (Figure 7B). Stiffness inhomogeneity in a location results in elevated stresses that span across adjacent walls. This may explain how, if one of the periclinal walls develops a particular pattern of anisotropy or inhomogeneity, the other wall is triggered to mirror it, such as through microtubule-mediated deposition of cellulose. The stress pattern would be propagated from one periclinal wall to the other through the anticlinal walls.

The 3D reconstruction of the z stacks shows that cortical microtubules assumed a preferentially vertical (z direction) orientation along the anticlinal walls (Figures 7C and 7D; Video S4), corroborating the stress anisotropy predicted by our FE model (Figure 2B). This suggests that turgor-driven stress overrides any putative "tissue-level" forces in the plane of the leaf. Distribution of microtubules along the anticlinal walls was non-uniform, and the microtubules were enriched near necks. The 3D visualization of microtubules (Videos S3, S4, and S5) and 3D reconstructions of dual-channel z stacks (Video S4) were helpful to determine the microtubule localization relative to the adjacent anticlinal wall, particularly for the early-stage bends (shallow bends marked in Video S5). Our analysis of microtubule density demonstrated that microtubules were mostly enriched on the neck sides of the anticlinal walls (p < 0.0001; see Figures S7F-1 and S7F-2, Video S5, and Quantification and Statistical Analysis), coinciding with microtubule bundles under periclinal wall necks. Thus, microtubule association with necks is not limited to periclinal walls, but also occurs along anticlinal walls.

Cell Wall Buckling May Precede Microtubule Polarization

We observed that microtubules form bundles in necks in regions with an already-established curvature and were scarce in lobes (Figure 7E). In smaller, less-developed cells or regions of walls with smaller bends, however, the difference in microtubule densities on two sides of the wall appeared to be significantly less pronounced, compared to later stages (Figure 7F). Plotting the difference in microtubule numbers on two sides of the wall against the degree of wall curvature (as a measure of lobe progression) revealed a moderate correlation (r = 0.5; see Figures S7E and S7G; Quantification and Statistical Analysis). This further supports the proposed notion that rather than being the initial trigger, microtubule bundling and consequent wall reinforcement may amplify the formed waves in a positive-feedback loop following an initial buckling event.

DISCUSSION

The analysis of the physiochemical underpinnings of pavement cell morphogenesis has presented a formidable challenge to biologists and modelers (Bidhendi and Geitmann, 2019a; Sapala et al., 2018; Sotiriou et al., 2018; Belteton et al., 2018; Majda et al., 2017; Armour et al., 2015; Sampathkumar et al., 2014; Zhang et al., 2011; Xu et al., 2010; Fu et al., 2005; Panteris and Galatis, 2005). Until now, experimental evidence on cell wall composition consistent with a mechanical model for the formation of interlocking patterns had remained scarce. Sampathkumar et al. (2014) analyzed the correlation between cell wall stress

and microtubule organization in pavement cells, albeit *post facto*, in cells that were already wavy, and they consolidated the existing knowledge and linked microtubule organization, cell shape, and mechanical stress. However, the origin of wavy cell shapes was not addressed. Here, we focused on events leading to wavy cell shapes *de novo.*

Our initial simulations, based on isolated anticlinal walls and previous work (Bidhendi and Geitmann, 2019a), have suggested that focusing solely on anticlinal walls can result in an inaccurate description of plant cell mechanics and wall stress state. Simulations including the periclinal walls, on the other hand, generated crucial and non-intuitive information. Because of the difference in wall surface areas between the combined periclinal walls and the anticlinal walls for dimensions typical for epidermal cells of *A. thaliana*, applying pressure to all walls causes the periclinal walls to bulge out and the anticlinal walls to be pulled inward, reducing the in-plane projected cell surface. These simulations also imply that for a cell to grow in-plane, selective and isotropic softening of the anticlinal walls is not sufficient, and changes in mechanical properties of periclinal walls and wall anisotropy are required.

The 3D cell models also showed that due to turgor, the anticlinal walls experience significant tensile stresses vertically (in the z direction), compared to the in-plane directions, supported by the net vertical orientation of cortical microtubules underlying the anticlinal walls. The vertical microtubules are expected to cause anisotropic reinforcement of anticlinal walls mediated by cellulose deposition starting at very early stages, upon formation and fusion of the cell plate. This anisotropic reinforcement enables the anticlinal walls to grow along their in-plane axis while limiting their out-of-plane expansion (Figures S7A−S7C). The models indicate that the alternately located, non-yielding (stiff) regions on periclinal walls develop into necks. We show that this is consistent with the pattern of cellulose deposition and pectin de-esterification. Once lobes and necks are initiated, the geometry itself acts as an enhancer of stress differentials, and elevated stresses are formed at the neck side even if uniform isotropic material properties are used. The stress pattern obtained for cells shaping *de novo* closely matches the experimental observations of cortical microtubule bundling and their orientation in necks. Our mechanical model can explain why interference with cortical microtubule bundling or cellulose synthesis can reduce pavement cell waviness (CGA treatment in the present study; Armour et al., 2015; Fujita et al., 2013; Fu et al., 2005; Mathur, 2004). It also predicts that interference with pectin de-esterification can affect the lobe formation in pavement cells. We demonstrate that developing lobes and necks can initiate from small stiffness differentials if a stress-stiffening mechanism with lateral inhibition is incorporated. The existence of such a lateral inhibition mechanism seems to find an immediate biological equivalent in the proposed antagonism between microtubule and actin regulation pathways (Chen et al., 2015; Xu et al., 2010; Fu et al., 2005, 2002), although these pathways and, specifically, the exclusivity of actin to lobes, are not uncontested (Belteton et al., 2018; Armour et al., 2015) and warrant further investigation. Interference with stress-sensing mechanisms or wall reinforcement at any level is predicted to result in shallow waves whose expansion is hampered, or even reversed, by

straightening upon cell growth. Consistent with these predictions, the fact that in all cases of pharmacological interference with actin and microtubules, at least a slight border waviness remains is explained by the spontaneous buckling of the walls, as will be discussed later.

Staining cotyledon pavement cells with COS[488] shows pectin to be weakly esterified at the neck sides. De-esterified pectin can increase the stiffness of the cell wall when cross-linked by calcium. The esterification status of pectin has been implied in other plant tissues related to the anisotropic growth of cells, cell shape deformations, and organogenesis (Carter et al., 2017; Majda et al., 2017; Bidhendi and Geitmann, 2016; Peaucelle et al., 2015; Braybrook and Peaucelle, 2013; Palin and Geitmann, 2012; Fayant et al., 2010; Wolf et al., 2009).

Calcofluor white and PFS staining revealed bundles of cellulose microfibrils radiating from the necks, which can cause locally elevated stiffness and restrict growth in these regions. Similar to the organization of microtubules, microfibrils seemed to connect the adjacent necks. In some observations, the neck-neck connections in the inner periclinal walls appeared to be more pronounced, and bundles of cellulose seemed more strongly defined, compared to the outer periclinal walls. Therefore, the inner periclinal wall may be more determinant in dictating the undulation patterns, while the outer periclinal wall may loosely mimic the cellulose pattern of the inner wall. Such harmonization is possible by stress and strain coupling through anticlinal walls. Alternatively, the observed stronger neck to neck associations in the inner periclinal walls may reflect a temporal order of events, with the formation of waves in one of the walls preceding the other.

Armour et al. (2015) reported that the regions of the anticlinal wall where microtubules form the cortical anticlinal bundles mark the positions of incipient necks. However, close analysis of their micrographs suggests that even the earliest evidence of microtubules focally marking a region of the anticlinal wall is associated with an already-existing local change of curvature, albeit shallow. Therefore, the available studies cannot indicate whether it was a change in the cell wall composition or stress that caused the bundling of the microtubules in those regions, or if it was the microtubule accumulation that defined the site of future bends. We noted that the change in microtubule density on the two sides of a wave is a gradual process and is imperceptible for slight wall curvatures. We suggest that the initial difference in microtubule density is a response to stress or strain symmetry breaking, rather than its cause. Our new hypothesis considers this stress or strain asymmetry to result from an event that forms slight waves in the cell walls: buckling. Buckling is a mechanical instability that occurs when structures lose their axial load-bearing capacity under compressive stress states, resulting in the formation of bends. We provide a proof of concept for the notion that buckling in the walls can simply result from cell geometry and turgor in the form of wrinkling or crimpling. Here, we suggest buckling to act as a morphogen and a polarizer leading to the spontaneous and stochastic formation of local stress hotspots. These can then trigger microtubule bundling and, acting in a positive-feedback loop, can cause cell wall reinforcement through

local cellulose deposition and changes in pectin chemistry (Figure 7G). This concept does not exclude that, independently, and compounding this effect, compressive stresses may arise due to conditions such as variations in growth rates between adjacent cells or wall segments. Armour et al. (2015) and Elsner et al. (2012) demonstrated that pavement cell growth rates can vary considerably over both inter- and intracellular scales. Further, as buckling of a structure depends not only on the magnitude of the axial compressive loads, but also on the geometrical aspects of that structure (e.g., wall thickness), we propose that the difference in dimensions of epidermal cells is one of the factors that influence how resilient they are against buckling, creating the great variation of waviness observed among pavement cells of different species (Vőfély et al., 2019).

Our proposed model, based on buckling as a mechanical event preceding cytoskeletal and cell wall polarization, also provides a conceivable explanation to a phenomenon that is subtle and hence typically neglected: the presence of residual undulations in specimens subjected to pharmacological treatments or mutations. Interference with the regulators of microtubule functioning such as brassinosteroids; regulators of ROPs such as RhoGDIs; and mutations in microtubule-associated or microtubule-severing proteins such as IQD, CLASP or KATANIN all considerably decrease, but in no case do they completely eliminate cell border undulations (Liang et al., 2018; Liu et al., 2018; Mitra et al., 2019; Möller et al., 2017; Akita et al., 2015; Han et al., 2015; Lin et al., 2013; Wu et al., 2013; Ambrose et al., 2011; Kirik et al., 2007; Kotzer and Wasteneys, 2006; Fu et al., 2005). The same applies to mutations or treatments affecting actin (Rosero et al., 2016; Le et al., 2006) or cellulose synthesis or crystallinity, such as in *any1* (Fujita et al., 2013; Ivakov and Persson, 2013) or our CGA treatments. Neither interference with cytoskeletal elements nor alteration of the wall composition has shown to result in a complete loss of waviness at cell borders. Such events can always be explained with redundancies and compensatory mechanisms, but our model raises a different hypothesis: while microtubules and subsequent cellulose reinforcement of the cell wall are crucial in pavement cell development and morphogenesis, they do not initiate cell border undulations, but rather establish and enhance them.

STAR★METHODS

Detailed methods are provided in the online version of this paper and include the following:

- KEY RESOURCES TABLE
- LEAD CONTACT AND MATERIALS AVAILABILITY
- EXPERIMENTAL MODEL AND SUBJECT DETAILS
  - Plant material and growth conditions
- METHOD DETAILS
  - Polysaccharide staining
  - Fluorescence microscopy
  - Image analysis and 3D reconstruction software
  - CGA treatment and time-lapse study of pavement cell growth
  - Computational models

- QUANTIFICATION AND STATISTICAL ANALYSIS
  - Microtubule localization
  - Pectin label signal intensity
  - Cellulose label signal intensity
  - Cell growth measurements
- DATA AND CODE AVAILABILITY

SUPPLEMENTAL INFORMATION

Supplemental Information can be found online at https://doi.org/10.1016/j.celrep.2019.07.006.

AUTHOR CONTRIBUTIONS

A.J.B. and A.G. designed the study. A.J.B. conducted the modeling and the experiments. F.P.G. advised on the modeling. B.A. provided the CGA treatment results. A.J.B., F.P.G, and A.G. analyzed the data and wrote the manuscript.

DECLARATION OF INTERESTS

The authors declare no competing interests.

REFERENCES

Akita, K., Higaki, T., Kutsuna, N., and Hasezawa, S. (2015). Quantitative analysis of microtubule orientation in interdigitated leaf pavement cells. Plant Signal. Behav. *10*, e1024396.

Ambrose, C., Allard, J.F., Cytrynbaum, E.N., and Wasteneys, G.O. (2011). A CLASP-modulated cell edge barrier mechanism drives cell-wide cortical microtubule organization in *Arabidopsis*. Nat. Commun. *2*, 430.

Amsbury, S., Hunt, L., Elhaddad, N., Baillie, A., Lundgren, M., Verhertbruggen, Y., Scheller, H.V., Knox, J.P., Fleming, A.J., and Gray, J.E. (2016). Stomatal function requires pectin de-methyl-esterification of the guard cell wall. Curr. Biol. *26*, 2899–2906.

Anderson, C.T., Carroll, A., Akhmetova, L., and Somerville, C. (2010). Real-time imaging of cellulose reorientation during cell wall expansion in *Arabidopsis* roots. Plant Physiol. *152*, 787–796.

Armour, W.J., Barton, D.A., Law, A.M., and Overall, R.L. (2015). Differential growth in periclinal and anticlinal walls during lobe formation in *Arabidopsis* cotyledon pavement cells. Plant Cell *27*, 2484–2500.

Baskin, T.I. (2005). Anisotropic expansion of the plant cell wall. Annu. Rev. Cell Dev. Biol. *21*, 203–222.

Baskin, T.I., Wilson, J.E., Cork, A., and Williamson, R.E. (1994). Morphology and microtubule organization in *Arabidopsis* roots exposed to oryzalin or taxol. Plant Cell Physiol. *35*, 935–942.

Baskin, T.I., Beemster, G.T., Judy-March, J.E., and Marga, F. (2004). Disorganization of cortical microtubules stimulates tangential expansion and reduces the uniformity of cellulose microfibril alignment among cells in the root of *Arabidopsis*. Plant Physiol. *135*, 2279–2290.

Belteton, S.A., Sawchuk, M.G., Donohoe, B.S., Scarpella, E., and Szymanski, D.B. (2018). Reassessing the roles of PIN proteins and anticlinal microtubules during pavement cell morphogenesis. Plant Physiol. *176*, 432–449.

Bidhendi, A.J., and Geitmann, A. (2016). Relating the mechanics of the primary plant cell wall to morphogenesis. J. Exp. Bot. *67*, 449–461.

Bidhendi, A.J., and Geitmann, A. (2018). Finite element modeling of shape changes in plant cells. Plant Physiol. *176*, 41–56.

Bidhendi, A.J., and Geitmann, A. (2019a). Geometrical details matter for mechanical modeling of cell morphogenesis. Dev. Cell *50*, 117–125.e2.

Bidhendi, A.J., and Geitmann, A. (2019b). Methods to quantify primary plant cell wall mechanics. J. Exp. Bot. *70*, 3615–3648.

Bidhendi, A.J., Altartouri, B., and Geitmann, A. (2015). Mechanics of interdigitating morphogenesis in pavement cells. Microsc. Microanal. *21*, 201–202.

Bou Daher, F., Chen, Y., Bozorg, B., Clough, J., Jönsson, H., and Braybrook, S.A. (2018). Anisotropic growth is achieved through the additive mechanical effect of material anisotropy and elastic asymmetry. eLife *7*, e38161.

Braybrook, S.A., and Peaucelle, A. (2013). Mechano-chemical aspects of organ formation in *Arabidopsis thaliana*: the relationship between auxin and pectin. PLoS ONE *8*, e57813.

Burgert, I., and Fratzl, P. (2009). Plants control the properties and actuation of their organs through the orientation of cellulose fibrils in their cell walls. Integr. Comp. Biol. *49*, 69–79.

Carter, R., Woolfenden, H., Baillie, A., Amsbury, S., Carroll, S., Healicon, E., Sovatzoglou, S., Braybrook, S., Gray, J.E., and Hobbs, J. (2017). Stomatal opening involves polar, not radial, stiffening of guard cells. Curr. Biol. *27*, 2974–2983.e2.

Chebli, Y., Kaneda, M., Zerzour, R., and Geitmann, A. (2012). The cell wall of the *Arabidopsis* pollen tube–spatial distribution, recycling, and network formation of polysaccharides. Plant Physiol. *160*, 1940–1955.

Chen, J., Wang, F., Zheng, S., Xu, T., and Yang, Z. (2015). Pavement cells: a model system for non-transcriptional auxin signalling and crosstalks. J. Exp. Bot. *66*, 4957–4970.

Cosgrove, D.J. (2005). Growth of the plant cell wall. Nat. Rev. Mol. Cell Biol. *6*, 850–861.

Cosgrove, D.J. (2016). Plant cell wall extensibility: connecting plant cell growth with cell wall structure, mechanics, and the action of wall-modifying enzymes. J. Exp. Bot. *67*, 463–476.

Cosgrove, D.J. (2018). Nanoscale structure, mechanics and growth of epidermal cell walls. Curr. Opin. Plant Biol. *46*, 77–86.

Crowell, E.F., Bischoff, V., Desprez, T., Rolland, A., Stierhof, Y.-D., Schumacher, K., Gonneau, M., Höfte, H., and Vernhettes, S. (2009). Pausing of Golgi bodies on microtubules regulates secretion of cellulose synthase complexes in *Arabidopsis*. Plant Cell *21*, 1141–1154.

Crowell, E.F., Timpano, H., Desprez, T., Franssen-Verheijen, T., Emons, A.-M., Höfte, H., and Vernhettes, S. (2011). Differential regulation of cellulose orientation at the inner and outer face of epidermal cells in the *Arabidopsis* hypocotyl. Plant Cell *23*, 2592–2605.

Dessault Systèmes Simulia Corp. (2014). Abaqus 6.14 Analysis User's Guide (Dassault Systèmes Simulia Corp.).

Elsner, J., Michalski, M., and Kwiatkowska, D. (2012). Spatiotemporal variation of leaf epidermal cell growth: a quantitative analysis of *Arabidopsis thaliana* wild-type and triple cyclinD3 mutant plants. Ann. Bot. *109*, 897–910.

Elsner, J., Lipowczan, M., and Kwiatkowska, D. (2018). Differential growth of pavement cells of *Arabidopsis thaliana* leaf epidermis as revealed by microbead labeling. Am. J. Bot. *105*, 257–265.

Eng, R.C., and Sampathkumar, A. (2018). Getting into shape: the mechanics behind plant morphogenesis. Curr. Opin. Plant Biol. *46*, 25–31.

Fayant, P., Girlanda, O., Chebli, Y., Aubin, C.-É., Villemure, I., and Geitmann, A. (2010). Finite element model of polar growth in pollen tubes. Plant Cell *22*, 2579–2593.

Fu, Y., Li, H., and Yang, Z. (2002). The ROP2 GTPase controls the formation of cortical fine F-actin and the early phase of directional cell expansion during *Arabidopsis* organogenesis. Plant Cell *14*, 777–794.

Fu, Y., Gu, Y., Zheng, Z., Wasteneys, G., and Yang, Z. (2005). *Arabidopsis* interdigitating cell growth requires two antagonistic pathways with opposing action on cell morphogenesis. Cell *120*, 687–700.

Fujita, M., Himmelspach, R., Ward, J., Whittington, A., Hasenbein, N., Liu, C., Truong, T.T., Galway, M.E., Mansfield, S.D., Hocart, C.H., and Wasteneys, G.O. (2013). The anisotropy1 D604N mutation in the Arabidopsis cellulose synthase1 catalytic domain reduces cell wall crystallinity and the velocity of cellulose synthase complexes. Plant Physiol. *162*, 74–85.

Geitmann, A., and Ortega, J.K. (2009). Mechanics and modeling of plant cell growth. Trends Plant Sci. *14*, 467–478.

Giannoutsou, E., Apostolakos, P., and Galatis, B. (2016). Spatio-temporal diversification of the cell wall matrix materials in the developing stomatal complexes of Zea mays. Planta *244*, 1125–1143.

Gu, Y., Kaplinsky, N., Bringmann, M., Cobb, A., Carroll, A., Sampathkumar, A., Baskin, T.I., Persson, S., and Somerville, C.R. (2010). Identification of a cellulose synthase-associated protein required for cellulose biosynthesis. Proc. Natl. Acad. Sci. USA *107*, 12866–12871.

Hamant, O., and Traas, J. (2010). The mechanics behind plant development. New Phytol. *185*, 369–385.

Hamant, O., Inoue, D., Bouchez, D., Dumais, J., and Mjolsness, E. (2019). Are microtubules tension sensors? Nat. Commun. *10*, 2360.

Han, B., Chen, L., Wang, J., Wu, Z., Yan, L., and Hou, S. (2015). Constitutive Expresser of Pathogenesis Related Genes 1 is required for pavement cell morphogenesis in *Arabidopsis*. PLoS ONE *10*, e0133249.

Ivakov, A., and Persson, S. (2013). Plant cell shape: modulators and measurements. Front. Plant Sci. *4*, 439.

Jacques, E., Verbelen, J.-P., and Vissenberg, K. (2014). Review on shape formation in epidermal pavement cells of the *Arabidopsis* leaf. Funct. Plant Biol. *41*, 914–921.

Kirik, V., Herrmann, U., Parupalli, C., Sedbrook, J.C., Ehrhardt, D.W., and Hülskamp, M. (2007). CLASP localizes in two discrete patterns on cortical microtubules and is required for cell morphogenesis and cell division in *Arabidopsis*. J. Cell Sci. *120*, 4416–4425.

Korn, R.W. (1976). Concerning the sinuous shape of leaf epidermal cells. New Phytol. *77*, 153–161.

Korn, R.W., and Spalding, R.M. (1973). The geometry of plant epidermal cells. New Phytol. *72*, 1357–1365.

Kotzer, A., and Wasteneys, G. (2006). Mechanisms behind the puzzle: microtubule–microfilament cross-talk in pavement cell formation. Botany *84*, 594–603.

Landrein, B., and Hamant, O. (2013). How mechanical stress controls microtubule behavior and morphogenesis in plants: history, experiments and revisited theories. Plant J. *75*, 324–338.

Le, J., Mallery, E.L., Zhang, C., Brankle, S., and Szymanski, D.B. (2006). *Arabidopsis* BRICK1/HSPC300 is an essential WAVE-complex subunit that selectively stabilizes the Arp2/3 activator SCAR2. Curr. Biol. *16*, 895–901.

Liang, H., Zhang, Y., Martinez, P., Rasmussen, C.G., Xu, T., and Yang, Z. (2018). The microtubule-associated protein IQ67 DOMAIN5 modulates microtubule dynamics and pavement cell shape. Plant Physiol. *177*, 1555–1568.

Liesche, J., Ziomkiewicz, I., and Schulz, A. (2013). Super-resolution imaging with Pontamine Fast Scarlet 4BS enables direct visualization of cellulose orientation and cell connection architecture in onion epidermis cells. BMC Plant Biol. *13*, 226.

Lin, D., Cao, L., Zhou, Z., Zhu, L., Ehrhardt, D., Yang, Z., and Fu, Y. (2013). Rho GTPase signaling activates microtubule severing to promote microtubule ordering in *Arabidopsis*. Curr. Biol. *23*, 290–297.

Liu, X., Yang, Q., Wang, Y., Wang, L., Fu, Y., and Wang, X. (2018). Brassinosteroids regulate pavement cell growth by mediating BIN2-induced microtubule stabilization. J. Exp. Bot. *69*, 1037–1049.

Majda, M., Grones, P., Sintorn, I.-M., Vain, T., Milani, P., Krupinski, P., Zagórska-Marek, B., Viotti, C., Jönsson, H., Mellerowicz, E.J., et al. (2017). Mechanochemical polarization of contiguous cell walls shapes plant pavement cells. Dev. Cell *43*, 290–304.e4.

Majda, M., Krupinski, P., Jönsson, H., Hamant, O., and Robert, S. (2019). Mechanical asymmetry of the cell wall predicts changes in pavement cell geometry. Developmental Cell *50*, 9.

Marc, J., Granger, C.L., Brincat, J., Fisher, D.D., Kao, Th., McCubbin, A.G., and Cyr, R.J. (1998). A GFP-MAP4 reporter gene for visualizing cortical microtubule rearrangements in living epidermal cells. Plant Cell *10*, 1927–1940.

Mathur, J. (2004). Cell shape development in plants. Trends Plant Sci. *9*, 583–590.

Mathur, J. (2006). Local interactions shape plant cells. Curr. Opin. Cell Biol. *18*, 40–46.

Mitra, D., Klemm, S., Kumari, P., Quegwer, J., Möller, B., Poeschl, Y., Pflug, P., Stamm, G., Abel, S., and Bürstenbinder, K. (2019). Microtubule-associated protein IQ67 DOMAIN5 regulates morphogenesis of leaf pavement cells in *Arabidopsis thaliana*. J. Exp. Bot. *70*, 529–543.

Möller, B., Poeschl, Y., Plötner, R., and Bürstenbinder, K. (2017). PaCeQuant: a tool for high-throughput quantification of pavement cell shape characteristics. Plant Physiol. *175*, 998–1017.

Mravec, J., Kračun, S.K., Rydahl, M.G., Westereng, B., Miart, F., Clausen, M.H., Fangel, J.U., Daugaard, M., Van Cutsem, P., De Fine Licht, H.H., et al. (2014). Tracking developmentally regulated post-synthetic processing of homogalacturonan and chitin using reciprocal oligosaccharide probes. Development *141*, 4841–4850.

Murashige, T., and Skoog, F. (1962). A revised medium for rapid growth and bio assays with tobacco tissue cultures. Physiol. Plant. *15*, 473–497.

Nakamura, M., Naoi, K., Shoji, T., and Hashimoto, T. (2004). Low concentrations of propyzamide and oryzalin alter microtubule dynamics in *Arabidopsis* epidermal cells. Plant Cell Physiol. *45*, 1330–1334.

Palin, R., and Geitmann, A. (2012). The role of pectin in plant morphogenesis. Biosystems *109*, 397–402.

Panteris, E., and Galatis, B. (2005). The morphogenesis of lobed plant cells in the mesophyll and epidermis: organization and distinct roles of cortical microtubules and actin filaments. New Phytol. *167*, 721–732.

Peaucelle, A., Wightman, R., and Höfte, H. (2015). The control of growth symmetry breaking in the *Arabidopsis* hypocotyl. Curr. Biol. *25*, 1746–1752.

Peng, L., Xiang, F., Roberts, E., Kawagoe, Y., Greve, L.C., Kreuz, K., and Delmer, D.P. (2001). The experimental herbicide CGA 325′615 inhibits synthesis of crystalline cellulose and causes accumulation of non-crystalline β-1,4-glucan associated with CesA protein. Plant Physiol. *126*, 981–992.

Rosero, A., Oulehlová, D., Stillerová, L., Schiebertová, P., Grunt, M., Žárský, V., and Cvrčková, F. (2016). *Arabidopsis* FH1 formin affects cotyledon pavement cell shape by modulating cytoskeleton dynamics. Plant Cell Physiol. *57*, 488–504.

Rounds, C.M., Lubeck, E., Hepler, P.K., and Winship, L.J. (2011). Propidium iodide competes with Ca$^{(2+)}$ to label pectin in pollen tubes and *Arabidopsis* root hairs. Plant Physiol. *157*, 175–187.

Sampathkumar, A., Krupinski, P., Wightman, R., Milani, P., Berquand, A., Boudaoud, A., Hamant, O., Jönsson, H., and Meyerowitz, E.M. (2014). Subcellular and supracellular mechanical stress prescribes cytoskeleton behavior in *Arabidopsis* cotyledon pavement cells. eLife *3*, e01967.

Sapala, A., Runions, A., Routier-Kierzkowska, A.-L., Das Gupta, M., Hong, L., Hofhuis, H., Verger, S., Mosca, G., Li, C.-B., Hay, A., et al. (2018). Why plants make puzzle cells, and how their shape emerges. eLife *7*, e32794.

Schneider, C.A., Rasband, W.S., and Eliceiri, K.W. (2012). NIH Image to ImageJ: 25 years of image analysis. Nat. Methods *9*, 671–675.

Shaw, S.L., Dumais, J., and Long, S.R. (2000). Cell surface expansion in polarly growing root hairs of *Medicago truncatula*. Plant Physiol. *124*, 959–970.

Smith, L.G. (2003). Cytoskeletal control of plant cell shape: getting the fine points. Curr. Opin. Plant Biol. *6*, 63–73.

Smith, L.G., and Oppenheimer, D.G. (2005). Spatial control of cell expansion by the plant cytoskeleton. Annu. Rev. Cell Dev. Biol. *21*, 271–295.

Sotiriou, P., Giannoutsou, E., Panteris, E., Galatis, B., and Apostolakos, P. (2018). Local differentiation of cell wall matrix polysaccharides in sinuous pavement cells: its possible involvement in the flexibility of cell shape. Plant Biol (Stuttg) *20*, 223–237.

Szymanski, D.B. (2014). The kinematics and mechanics of leaf expansion: new pieces to the *Arabidopsis* puzzle. Curr. Opin. Plant Biol. *22*, 141–148.

Torode, T.A., O'Neill, R., Marcus, S.E., Cornuault, V., Pose, S., Lauder, R.P., Kračun, S.K., Rydahl, M.G., Andersen, M.C.F., Willats, W.G.T., et al. (2018). Branched pectic galactan in phloem-sieve-element cell walls: implications for cell mechanics. Plant Physiol. *176*, 1547–1558.

Vőfély, R.V., Gallagher, J., Pisano, G.D., Bartlett, M., and Braybrook, S.A. (2019). Of puzzles and pavements: a quantitative exploration of leaf epidermal cell shape. New Phytol. *221*, 540–552.

Watson, R. (1942). The effect of cuticular hardening on the form of epidermal cells. New Phytol. *41*, 223–229.

Wolf, S., Mouille, G., and Pelloux, J. (2009). Homogalacturonan methyl-esterification and plant development. Mol. Plant *2*, 851–860.

Wu, Y., Zhao, S., Tian, H., He, Y., Xiong, W., Guo, L., and Wu, Y. (2013). CPK3-phosphorylated RhoGDI1 is essential in the development of *Arabidopsis* seedlings and leaf epidermal cells. J. Exp. Bot. *64*, 3327–3338.

Xu, T., Wen, M., Nagawa, S., Fu, Y., Chen, J.-G., Wu, M.-J., Perrot-Rechenmann, C., Friml, J., Jones, A.M., and Yang, Z. (2010). Cell surface- and rho GTPase-based auxin signaling controls cellular interdigitation in *Arabidopsis*. Cell *143*, 99–110.

Yanagisawa, M., Desyatova, A.S., Belteton, S.A., Mallery, E.L., Turner, J.A., and Szymanski, D.B. (2015). Patterning mechanisms of cytoskeletal and cell wall systems during leaf trichome morphogenesis. Nat. Plants *1*, 15014.

Zhang, C., Halsey, L.E., and Szymanski, D.B. (2011). The development and geometry of shape change in *Arabidopsis thaliana* cotyledon pavement cells. BMC Plant Biol. *11*, 27.

STAR★METHODS

KEY RESOURCES TABLE

REAGENT or RESOURCE	SOURCE	IDENTIFIER
Chemicals, Peptides, and Recombinant Proteins		
Calcofluor White (Fluorescent Brightener 28)	Sigma-Aldrich	Cat# F6259
CGA 325′615 (CGA)	Syngenta (Basel, Switzerland)	N/A
COS[488]	Mravec et al., 2014	N/A
MES	Fisher Scientific	Cat# BP300-100
Murashige and Skoog Medium	Fisher Scientific	Cat# ICN2623220
Pontamine Fast Scarlet 4B (Direct Red 23)	Sigma-Aldrich	Cat# 212490-50G
Propidium iodide (PI)	Sigma-Aldrich	Cat# P4170-100MG
Experimental Models: Organisms/Strains		
Arabidopsis: Col-0	ABRC	CS70000
Arabidopsis: GFP-TUB6	ABRC	CS6550
Arabidopsis: GFP-MAP4	Charles Anderson lab	N/A
Software and Algorithms		
Abaqus	Dassault Systèmes, Simulia Corp.	https://www.3ds.com/products-services/simulia/products/abaqus/
Amira 5.6	Thermo-Fisher Scientific	https://www.thermofisher.com/us/en/home/industrial/electron-microscopy/electron-microscopy-instruments-workflow-solutions/3d-visualization-analysis-software/amira-life-sciences-biomedical.html
Bitplane Imaris 7.5.2	Bitplane	https://imaris.oxinst.com
Excel	Microsoft Corp.	https://products.office.com/en-us/excel
ImageJ / Fiji	Schneider et al., 2012	https://imagej.nih.gov/ij/; https://fiji.sc
Kappa plugin	Kevan Lu and Hadrien Mary, Gary Brouhard laboratory	https://github.com/brouhardlab/Kappa
Python 2.7.13 custom script	This paper	N/A

LEAD CONTACT AND MATERIALS AVAILABILITY

Further information and requests for resources and reagents should be directed to, and will be fulfilled by, the Lead Contact, Anja Geitmann (geitmann.aes@mcgill.ca).

EXPERIMENTAL MODEL AND SUBJECT DETAILS

Plant material and growth conditions

Arabidopsis thaliana is a widely used model plant. In this study, we used *Arabidopsis thaliana* ecotype Col-0 and the GFP-expressing lines GFP-MAP4 (Marc et al., 1998) and GFP-TUB6 (Nakamura et al., 2004). GFP-TUB6 expressing GFP-β-tubulin-6, obtained from *Arabidopsis* Biological Resource Center under stock number CS6550, was used to study microtubule localization in the pavement cells of cotyledons. The GFP-MAP4 line, with the GFP-labeled microtubule-binding domain (MBD) of the mammalian microtubule-associated protein (MAP4), was kindly provided by Dr. Charles Anderson and used to verify the observations with GFP-TUB6. For stratification, seeds were first gently agitated in 100% EtOH for 15 s, washed with double-distilled autoclaved water and submerged in 50% commercial bleach while being gently agitated for 5 min. After washing for 3-5 times with double-distilled autoclaved water, the seeds were stored in dark at 4°C for 3-4 days. *Arabidopsis* seeds were germinated in sterile Petri plates containing 1X MS (Murashige and Skoog, 1962) media with 1% sucrose and 0.8% plant agar under long-day (16h) lighting condition.

METHOD DETAILS

Polysaccharide staining

Staining procedures were carried out mostly in the dark. For visualizing cellulose, calcofluor white (Fluorescent Brightener 28, Sigma-Aldrich) and PFS (Pontamine Fast Scarlet 4B, now Direct Red 23, Sigma-Aldrich), a dye with a high affinity to cellulose (Liesche et al., 2013; Anderson et al., 2010), were used. Calcofluor was used at a concentration of 2 mg/mL in ddH$_2$O. PFS staining was carried out with a 14 mg/mL solution of PFS in PBS buffer (Na$_2$HPO$_4$ 3.2 mM, KH$_2$PO$_4$ 0.5 mM, NaCl 135 mM, KCl 1.3 mM, pH 7.3). Seedlings were placed in Eppendorf tubes containing calcofluor white and transferred to a vacuum of 20 in Hg (Pelco BioWave 34700) at room temperature. After 45 min the tubes were transferred to a rotator in a dark room for an additional 45 min. The specimens were then washed gently for 3-5 times with ddH$_2$O before being mounted in ddH$_2$O for observation. PFS staining was performed as described above for an incubation time of 30-60 min before washing and mounting in PBS for observation.

For pectin, seedlings were stained with either COS[488] or propidium iodide. COS[488] (Mravec et al., 2014) was generously provided by Dr. Jozef Mravec from the lab of Dr. William George Tycho Willats (University of Copenhagen). For COS[488] staining, the stock was diluted 1:500 in MES buffer (25 mM, pH 5.7). The seedlings were incubated with COS[488] for 5-15 min and washed with MES for 3-5 times for at least 30 s. The samples were then mounted in MES before visualization. For propidium iodide staining, seedlings were stained with 0.5 mg/mL solution of propidium iodide in double-distilled water (ddH$_2$O). A drop of propidium iodide was placed on each seedling. The dye was removed after 10-20 min with a Kimwipe tissue paper and the samples were washed gently with double-distilled water (ddH$_2$O) at least three times before mounting in water for visualization.

Fluorescence microscopy

Fluorescence microscopy was carried out on a Zeiss LSM 510 META confocal laser scanning microscope using a Plan Apochromat 63x oil immersion objective with numerical aperture of 1.40. For propidium iodide and PFS, excitation wavelength of 532 nm and bandpass emission filter of 550-615 nm were used. For COS[488], 489 nm laser with bandpass filter of 550-615 nm were used. For calcofluor white, excitation wavelength of 405 nm in META mode and bandpass filter of 420-480 nm were used. For GFP lines, either excitation wavelength of 489 nm with emission bandpass of 500-525 nm, or in META mode, the argon laser of 488 nm with bandpass filter of 505-550 nm were used. For time-lapse imaging of CGA-treated and control samples with propidium iodide staining, LSM 5 LIVE was used with 532 nm laser with 590-625 nm emission filter.

Image analysis and 3D reconstruction software

Analysis of fluorescence intensity was performed in ImageJ (Schneider et al., 2012) using the maximum projections of z stacks and for Figures 5D and S5F, the re-slicing and orthogonal viewing capabilities. 3D reconstruction of confocal z stacks was carried out using either Amira 5.6.0 (Thermo Fisher Scientific) or Bitplane Imaris 7.5.2 (Bitplane). Supplemental Videos were created using z stacks acquired by confocal laser scanning with the volumetric rendering function of Imaris software. For measurements and statistical analysis pertaining to cell wall components or microtubules refer to Quantification and Statistical Analysis.

CGA treatment and time-lapse study of pavement cell growth

The herbicide CGA (CGA 325′615) was generously provided by Syngenta (Basel, Switzerland). *Arabidopsis* cotyledon samples were treated with a 0.9 nM CGA concentration prepared from a 10 μM stock solution dissolved in DMSO. CGA is suggested to inhibit the synthesis and reduce the cell wall content of crystalline cellulose (Peng et al., 2001). The same concentration of DMSO (v/v) was used for the control experiment. The solutions were added to the 1/2 x MS (Murashige and Skoog, 1962) growth media. The samples were labeled with propidium iodide (0.01 mg/ml) for 20 min, followed by three washes with distilled water before observation. Propidium iodide labeling was applied at each time point prior to observation. At each acquisition, samples were mounted between slide and coverslip and placed immediately back to the *in vitro* growth chamber thereafter. At each time point, the same cells were located and traced. The adaxial side of the wild-type *Arabidopsis* was chosen for the study. For data analysis, see Quantification and Statistical Analysis and Figure S8.

Computational models
Material and model inputs

For all simulations (except for the buckling analysis as discussed later), Neo-Hookean hyperelastic material model was used to define the cell wall elastic behavior. Hyperelastic models are defined by strain energy potential functions. For Neo-Hookean hyperelastic material model, from Abaqus user manual, the strain energy potential, $U(\varepsilon)$ is defined as:

$$U = C_{10}(\bar{I}_1 - 3) + \frac{1}{D_1}(J^{el} - 1)^2$$

Where U is the strain energy per unit of reference volume, C_{10} and D_1 are material parameters and $\bar{I}_1$ is the first deviatoric strain invariant:

$$\bar{I}_1 = \bar{\lambda}_1^2 + \bar{\lambda}_2^2 + \bar{\lambda}_3^2$$

$\overline{\lambda_i}$ are the deviatoric stretches, $\overline{\lambda_i} = J^{-\frac{1}{3}}\lambda_i$. λ_i are the principal stretches. J is the total volume ratio. J^{el} is elastic volume ratio. The constants C_{10} and D_1 are required to define the Neo-Hookean hyperelastic model in Abaqus:

$$C_{10} = \frac{\mu_0}{2}$$

and

$$D_1 = \frac{2}{K_0}$$

μ_0 and K_0 correspond to initial shear and bulk moduli, respectively. We constructed our FE models based on normalized (dimensionless) inputs. Dimensionless values facilitate assessing the model's behavior without the need to operate on very small numbers that arise due to microscale dimensions of the geometries. This also reduces the possible round-off errors that may arise due to operations on very small numbers during numerical calculations. The material constants were normalized by μ_0. Therefore, for instance, for a region with default stiffness, a $C_{10} = 0.5$ could be used. Reduced or increased stiffness values were similarly assigned by values less or more than $C_{10} = 0.5$, respectively. Values of C_{10} used to test the behavior of the models varied between 5×10^{-2} and 50. The material in all models was considered incompressible. For such a case, $D_1 = 0$. It should be noted, however, that compressibility would not affect the overall behavior. The turgor was always applied as a distributed pressure on internal faces of the cell walls. The turgor input was also normalized by μ_0 (same units). The range of dimensionless values used for the pressure varied between 1×10^{-5} to 1×10^{-2}.

The cell dimensions were also normalized with respect to one of the dimensions. The base value for cell wall thickness was estimated as 700 nm from micrographs and was rounded up to 1 μm. The height of the anticlinal wall and its length were also approximated to 10 and 100 μm, respectively. For solid models, the normalized thickness, height, and length of the model with only the anticlinal wall included were 0.01, 0.1 and 1, respectively. For shell models with a piece of the cell wall containing multiple lobes and necks or for whole-cell models, these dimensions were 0.1, 1 and 10, maintaining the same aspect ratio.

To compare deformations in *ab initio* or *cum tempore* stiffening models, the secondary onset of stiffening in a segment of cell walls in the *cum tempore* model was applied indirectly through exploiting a temperature-dependent stiffness scenario. As temperature can be defined to change in time, the stiffness could be made to vary with time by defining temperature-dependent elastic constants. Quantitative comparisons between *ab initio* and *cum tempore* stiffening were performed by monitoring the displacement of four fiducial points on the 2D shell model (Figure S2C). The results indicate that, as expected, in both cases similar displacements for anticlinal and periclinal walls result from the application of pressure (Figures S2E and S2F).

Finite element implementation

For the model including only the anticlinal wall, continuum three-dimensional large-strain quadratic reduced-integration hybrid elements (C3D20RH) were used. The anticlinal walls of two adjacent cells were tied together in all degrees of freedom. For beam models, linear two-node beam elements were used. In other models, the cell wall was considered as a thin shell as the thickness of the cell wall compared to other cell dimensions is negligible. These models were discretized with four-node first-order reduced-integration shell elements (S4R). In multi-cell models, the geometries of individual cells were merged at their anticlinal walls. Boundary conditions were applied to allow free deformation of wall segments under pressure while preventing rigid body motion. Abaqus 6.14-2 FE package was used to create the geometries, for meshing and post-processing. Abaqus/Standard solver was used for quasi-static FE simulations (see Abaqus 6.14 Analysis User's Guide [Providence, RI: Dassault Systèmes Simulia Corp].Dessault Systèmes Simulia Corp., 2014).

Model of epidermis from confocal micrograph

The FE model of the epidermis with realistic cell shapes was constructed by extracting the cell borders from confocal micrographs of *Arabidopsis* cotyledon pavement cells stained with propidium iodide. First, 3D anticlinal walls were created by extruding the epidermal cell borders to a height of 10 μm, a typical value for *Arabidopsis* pavement cells. Outer periclinal walls were added by merging a shell plate to the anticlinal walls. The pressure was then applied to the inner face of the individual periclinal walls. Pressure was not applied on anticlinal walls as, being equal for all cells, pressures on two sides cancel each other out. Boundary condition on the lower end of the anticlinal walls was set to allow in-plane and prevent out-of-plane displacements. Displacements at the border of the epidermis model were constrained. Simulations show high tensile stresses to occur at the neck regions of the undulations and in the central regions of periclinal walls. The magnitude of stress in the central regions appears to correlate with the radius of the largest embeddable circle in that region, consistent with Sapala et al. (2018).

Anticlinal wall models

The border undulations in pavement cells as seen from above correspond to the edge forming the junction between the anticlinal and periclinal walls. Many studies have focused predominantly on waviness of the anticlinal walls. While such simplification can be acceptable in some cases, depending on the nature of the question being investigated, it can also result in misrepresentation of the cell mechanics and morphogenesis. We have previously shown that a model proposed by Majda et al. (2017, 2019) for wavy anticlinal walls based on stretch of the anticlinal walls by "tissue tension" results in conflicting outcomes (Bidhendi and Geitmann, 2019a). Here we design a model that allows assessing two other mechanisms focusing on the anticlinal wall that have the potential to form wavy cell walls: differential turgor between cells and differential growth in adjacent anticlinal wall layers.

An FE model simulates a section of anticlinal wall between two adjacent cells (Figure S1A) consisting of two layers (the primary walls of the two adjacent cells) glued together representing the middle lamella. Assigning different growth rates by assigning different coefficients of thermal expansion for each layer curves the bilayer. The layer with a higher expansion rate forms the convex (neck) side (Figure S1B). As the neck is thought to be restricted in growth by cellulose microfibrils (e.g., see Figure 6; Videos S1 and S2), this model seems therefore unphysiological.

To examine how differential turgor between neighboring cells deforms the anticlinal walls, hexagonal cell geometry is implemented (Figure S1C). As above, non-slipping non-separable contact is considered between the anticlinal walls of two cells. Pressure is exerted on the internal faces of anticlinal walls. At equal pressures, the midline of the shared anticlinal wall does not displace as the forces cancel each other out and only compress the wall. If differential pressures are applied, the anticlinal wall curves into the cell with lower pressure (Figure S1D). A more spatially confined deformation similar to a lobe protrusion can be achieved if the anticlinal wall layers are made locally softer on both sides (Figures S1E and S1F). Pavement cells form several necks and lobes in any given wall segment connecting two neighbors. Therefore, this model is also inconsistent with the biology, as it requires neighboring cells to switch pressures to form multiple protrusions and indents. Further, as explained in the next sections and in the main text, considering the full geometry of the cells with periclinal and anticlinal walls shows that results of this model, both in terms of deformations and stress orientation are irrelevant (Figures 2A–2D and S1G–S1K).

3D model of hexagonal pressurized cells

To examine the full cell geometry under pressure, we added the periclinal walls to the anticlinal wall model described in the previous section (Figures 2A and S1G). The solid model is discretized by continuum three-dimensional large-strain quadratic reduced-integration hybrid elements (C3D20RH). Wall thickness is identical for both anticlinal and periclinal walls, and the material is isotropic and uniform. The pressure in one cell is set higher (Figures S1I and S1K). As described in the main text, upon application of the pressure, cells initially swell out of the plane and the free anticlinal walls move inward, reducing the in-plane projected cell surface (Figures 2D and S1G–S1J). These models allowed examining the stress anisotropy in anticlinal walls (Figures 2B and 2C). They also allowed examining how softening of the anticlinal walls either locally or entirely affects its deformation (Figure S1J), compared to models without periclinal walls. Softening of the whole or a segment of the anticlinal wall shared between the cells also does not produce any wave at the superficial borders of the cells and any deformation remains limited to the anticlinal walls. Therefore, for the isotropic cell walls we tested, a pressure differential between cells cannot underlie lobe formation. Increasing the pressure or uniform softening of the anticlinal walls also does not increase the in-plane size of the cell.

Buckling model

Proof-of-concept buckling models were developed to demonstrate that the cell walls, including both the anticlinal and periclinal walls, can buckle resulting in wavy cell contours. For this, the cell was modeled as a hollow rectangular box (Figure 2E). Shell behavior was considered for the cell walls. Linear elastic material was used for linear buckling analysis. We observed that with and without a static preloading pressure step, the structure can buckle under internal pressure and positive eigenvalues exist for the buckling analysis. The eigenvalues of a buckling analysis depend on the geometry, dimensions, and material inputs as well as the boundary conditions. Figure 2E is from a model with dimensions of 100, 10 and 1 μm for length, height, and shell thickness of the model, respectively. The material is linear elastic with Young's modulus of 1 MPa and Poisson's ratio of 0.3. Boundary conditions are applied to prevent in or out of plane displacement of the inner (lower) periclinal walls (as attached to mesophyll cells). However, the outcome in terms of feasibility of buckling is not dependent on this particular boundary condition. Pressure load is applied to inner faces of outer periclinal walls. For these inputs, critical buckling load for pressure is as low as 2.8 kPa which is well below the reported range for turgor in plant cells.

Models with differential stiffness in the periclinal walls

The boundary conditions imposed on this class of models serve to enable horizontal (in x-direction) movement for the lower end of the anticlinal wall, including point A2 which represents the midpoint of the anticlinal wall. The periclinal end-points (P1 and P2 in beam model of Figure S2A and shell model of Figure 3B) can only move in the z-direction. The point corresponding to the connection of the anticlinal wall with the periclinal walls (A1) may move in all directions. These boundary conditions are applied in all similar models, including the models with alternately placed stiffness on periclinal walls. The displacement of the mid-point of the anticlinal wall is obtained from the output of the FE models as a measure of evolution and magnitude of a protrusion or lobe. In these simulations, the stiffness differential is implemented *ab initio*—prior to application of the pressure. As described in the Material and model inputs, the simulations reveal that it does not matter for the outcome whether the cells are under turgor (*cum tempore* stiffening) or relaxed (*ab initio* stiffening) when the stiffening is implemented (Figures S2C–S2F).

To rule out the dependence of models on the choice of turgor pressure, differential pressure is applied to the two adjacent cell walls. The results show that regardless of the relative pressures, the anticlinal wall is displaced toward the cell with the stiffer periclinal wall (Figure S3) as it deforms less under tension. In extreme conditions, when the pressure on the stiffened side approaches zero, the horizontal (in x-direction) displacement of the anticlinal wall becomes negligible (Figures S3E and S3F).

We tested different stiffness ratios between the stiffened and default periclinal walls and the resultant displacement of the anticlinal wall is monitored. In the model tested, as the stiffness ratio increases from 1 to 5, the displacement of the anticlinal wall increases rapidly, but beyond this value the deformation plateaus (Figure S4A). At this point, the stiffer side behaves as a rigid structure compared to the softer (lobe) side. Unless pressure is increased, any additional stiffness in the stiffer side does translate to a perceivable increase in horizontal (in x-direction) displacement of the anticlinal wall. We then tested whether subtle stiffness differentials

would eventually lead to undulations if the load is applied repeatedly. Iterative load application is accomplished by repeating the simulation starting off with the deformed shape of the previous step and re-zeroing the stress. Running the simulation for 3 iterations shows that the resulting horizontal (in x-direction) displacement of the anticlinal wall is negligible compared to the vertical (out of epidermis plane, in z-direction) deformation (Figure S4B). Therefore, when continued, the cells only balloon out of the plane, not forming discernable undulations. This demonstrates that repeated load application does not cause more pronounced wave formation if the stiffness difference is negligible initially and is set to remain constant. In such a case, a sufficiently large stiffness ratio between the two periclinal wall segments is required (Figure S4C).

In models with alternatingly placed stiff regions, the stiffening bands on periclinal walls are extended in the depth of the anticlinal walls. Equal pressures are applied under periclinal walls on both sides of the shared anticlinal wall (Figure 3E). Similar to earlier models, to assess lobe formation, horizontal (in x-direction) displacement of the mid-point of the anticlinal wall (A2) is recorded in each simulation (Figure 3F). Inclusion of softened regions between the stiffenings followed a similar modeling procedure. The simulations indicate that in the presence of periclinal wall stiffenings, undulations can be generated without stiffening in the anticlinal wall, but the magnitude of the undulations is reduced in absence of the latter as measured by the relative displacement of point A2 (Figures 3J and 3K). Relatedly, stiffness bands on anticlinal wall in the absence of alternating stiffness regions on the periclinal walls cannot produce lobes under application of pressure.

Stress-stiffening feedback loop

To implement the stress-stiffening feedback loop, a custom Python script was used to read data from and write data to the FE model (Figure S6). After each iteration, the code extracts the deformed geometry from the Abaqus database and reads the stresses for each element. If a specific element has a stress higher than a threshold and does not belong to a list of the stiffening-inhibition zone (in the model accounting for inhibition of stiffening), the new value of stiffness for that element in terms of C_{10} is updated according to $C_{10_{new}} = C_{10_{old}} + \tanh(C_{10_{old}} \times S_{rel})$; where S_{rel} is the von Mises stress of the corresponding element relative to the threshold stress. The threshold stress was set in each iteration as the average stress of all elements. Otherwise, $C_{10_{new}} = C_{10_{old}}$ was assigned for the element with either a stress below the threshold stress or located in a stiffening-exclusion zone for the feedback loop with inhibition of stiffening in between incipient necks. After assigning new stiffness values, the script runs the model keeping constant all other model parameters such as the pressure and boundary conditions. It is worth noting that, in these simulations, we started from straight cell borders and did not incorporate the initial small waves that we suggest to arise due to cell wall buckling. When small initial waves are incorporated, the appearing stress on the neck side due to geometry might be sufficient to prevent leveling out the stress inhomogeneity and the need for a stiffening inhibition mechanism between developing necks.

QUANTIFICATION AND STATISTICAL ANALYSIS

Microtubule localization
Cortical microtubules at the periclinal wall

Periclinal microtubule density was compared between necks and lobes of pavement cells. This was carried out by reading the mean signal intensity in a circle with a consistent area (8.5 μm^2) placed on two sides of the cell border of a wave (Figure S7D). z stacks of pavement cells of GFP-TUB6 line were acquired for cotyledons of seedlings at 2-5 DAG. The depth of z-scanning was typically between 10 to 20 μm and was adjusted for each z stack by determining the first and last slices of the stack to ensure that the outer periclinal walls, the entire height of anticlinal walls, and at least some portion of the inner periclinal walls were captured to allow for a 3D view of the cell structures. This approach allowed us to later dissect the z stacks and study the outer periclinal walls and the anticlinal walls separately. For each micrograph used in the analysis, a slide was determined from the z stack that contained all cell borders (top of the anticlinal walls) with little to no periclinal wall signal showing. These particular sections were pseudocolored orange/red to mark the cell borders (e.g., Figure S7D). To collapse the periclinal wall information into a single image, maximum projection of the fluorescence signals from the first optical section down to the specific section chosen as the beginning of the anticlinal wall was made and pseudocolored yellow. The borders colored red/orange and the max projection data from the periclinal wall were merged into a single micrograph as depicted in Figure S7D. These micrographs were used to compare signal intensity on the opposing sides of borders in circular regions of interests on necks and lobes (Figure S7D). The analyzed population was n = 6 pavement cells from n = 6 cotyledons. From these n = 84 lobe and neck pairs were analyzed. The mean signal intensity was mostly higher on the neck side and t test carried out on all the pairs indicated a significant difference (p < 0.0001). This analysis corresponds to Figures 6B, 6C, and S7D.

Cortical microtubules at the anticlinal wall

The abundance of microtubules at the neck and lobe sides of the anticlinal walls was determined by counting the cortical anticlinal microtubules on each side. This was carried out using 3D reconstructions of z stacks of GFP-MAP4 line cotyledons between at 2-5 DAG. Specifically, using overlapping double-channel 3D reconstructions marking microtubules (GFP-MAP4) and cell wall polysaccharides (propidium iodide) allowed us to ascertain whether a given microtubule array lined the neck or the lobe side of a segment of the anticlinal wall (Video S4; Figure S7F). We analyzed n = 34 lobe and neck pairs from n = 9 pavement cells randomly selected from z stacks of n = 3 cotyledons of the GFP-MAP4 line. Paired t test showed that the microtubule population is consistently denser on the neck sides (p < 0.0001). This analysis is mentioned in the legend of Figure 7D. Further, from the same data, segments with an arc length of 6 μm were selected choosing points on the cell borders on maximum projection micrographs using Fiji (Fiji Is Just ImageJ)

plugin Kappa (developed by the Brouhard laboratory, brouhardlab.mcgill.ca) (segments of the anticlinal walls, Figure S7E). A B-spline was fitted to the selected points. Kappa provides the length of the chosen arc and its average curvature. Curvature is $\frac{1}{R}$, where R is the radius of a circle fitted to the arc. The analysis was carried out on a range of wall segment curvatures starting from relatively straight borders to rather pronounced lobes. We observed a moderate correlation (r = 0.5) when the relative difference in microtubule number between necks and lobes in percentage $((N_{neck} - N_{lobe}/N_{neck}) \times 100)$ was plotted against segment curvatures (Figure S7G). Pronounced bends showed a higher difference in microtubule numbers on the two opposing sides of the anticlinal wall. Obviously, the progression of a lobe does not depend on line curvature alone and further studies could consider the depth (base to tip length) of the lobes in addition to their curvature for a more thorough analysis of the correlation between shape, stage of the wall curvature and microtubule polarization. However, this was beyond the scope of the present paper. The scoring of microtubule location with respect to neck or lobe side of the anticlinal wall was based on the position relative to the anticlinal wall, corroborated by the fact that the arrays continued from the anticlinal wall to radiate under the periclinal wall of the respective cell. This was particularly obvious in neck regions (see Videos S3–S5).

Pectin label signal intensity

COS[488], highly specific to weakly esterified pectin (Mravec et al., 2014), was used to stain pectin. Using ImageJ, maximum signal intensity projections were obtained from confocal z stacks. Similar to analyses in the previous section for microtubules along the periclinal wall, circles were placed on two sides of a wave on necks and lobes to compare signal intensity from COS[488] staining (Figure S7H). The area of the circle was kept constant between all measurements (5 μm^2). Images of n = 5 cotyledons from n = 5 seedlings were chosen and from each cotyledon n = 1-2 pavement cells were analyzed for COS[488] signal, making in total n = 55 pairs of neck and lobe measurements. The paired t test showed a significant difference as necks appeared consistently brighter than lobes (p < 0.0001). Figures 5A−C is related to results from this analysis.

Analysis of propidium iodide signal intensity for pectin staining was carried out as described above for COS[488] staining. n = 5 cotyledons from different staining experiments were used and from each between n = 3 to 5 pavement cells were chosen for analysis making up to n = 19 cells and n = 101 lobe and neck pairs analyzed. Signal intensities obtained for necks were ubiquitously higher than lobes and the differences were significant as determined by paired t tests (p < 0.0001). Figure 5D corresponds to results from this analysis.

Cellulose label signal intensity

Calcofluor white (Fluorescent Brightener 28, Sigma-Aldrich) and Pontamine Fast Scarlet 4B (PFS, now termed as Direct Red 23; Sigma-Aldrich) were used to label cellulose, as described in the polysaccharide staining section of the Method Details. Labeling cotyledon pavement cells, fibrillar bundles of cellulose were prominent, fanning out on the indentation (neck) sides (Figures 6D−6G, S5F, and S5H for calcofluor white and Figures S5D and S5E for PFS. Also see Videos S1 and S2). This pattern was similar to the observed microtubule enrichment in the necks under periclinal walls. Extension of cellulose enrichment at locations of necks could also be observed to reach into the depth of the anticlinal walls (Figures 6L, S5F-1, and S5F-2; Videos S1 and S2). To ensure that this observation is consistent, signal intensities in maximum z projections were compared between necks and lobes of periclinal walls in PFS stained samples since this dye is suggested to be highly specific in binding cellulose (Liesche et al., 2013; Anderson et al., 2010). Similar to the measurements described above for pectin, this was carried out by placing circular regions of interest in which mean signal intensities were read and compared. n = 6 cells from n = 3 seedlings were selected from which n = 88 lobe and neck pairs were analyzed. A paired t test showed a significant difference between signal intensities of necks and lobes (p < 0.0001). This analysis is mentioned in the legend for Figure 6.

Cell growth measurements

In order to determine the effect of CGA application on pavement cell shape, cell circularity, area, and perimeter were measured from time-lapse data acquired at two time points between 2 and 4 DAG. Cell perimeters were traced manually in ImageJ, on the z stack projection of the cells. To ensure the highest possible precision, we eschewed the use of automated algorithms but instead counted lobe numbers manually (the "gold standard" against which most automated algorithms are compared). The analysis was conducted on n=50-70 cells from n=10-12 seedlings to produce each data point. A paired t test showed a significant difference in the lobe number between the control and treated cells (p<0.001). Details of CGA treatment can be found under Method Details. Analysis results can be seen in Figure S8.

DATA AND CODE AVAILABILITY

A Python script was used to read data from the FE model, to update the data and to re-run the model in a loop. The script is available upon request.